J. Plasma Phys. (2025), *vol*. 91, E147
 doi:10.1017/S0022377825100883

Modelling cosmic-ray transport: magnetised versus unmagnetised motion in astrophysical magnetic turbulence

Jeremiah Lübke[1], Patrick Reichherzer[2], Sophie Aerdker[3], Frederic Effenberger[1,3], Mike Wilbert[1], Horst Fichtner[3] and Rainer Grauer[1]

[1]Institut für Theoretische Physik I, Ruhr-Universität Bochum, 44801 Bochum, Germany
[2]Department of Physics, University of Oxford, Oxford OX1 3PU, UK
[3]Institut für Theoretische Physik IV, Ruhr-Universität Bochum, 44801 Bochum, Germany
Corresponding author: Jeremiah Lübke, jeremiah.luebke@rub.de

(Received 23 May 2025; revision received 7 August 2025; accepted 8 September 2025)

Cosmic-ray transport in turbulent astrophysical environments remains a multifaceted problem and, despite decades of study, the impact of complex magnetic field geometry – evident in simulations and observations – has only recently received more focussed attention. To understand how ensemble-averaged transport behaviour emerges from the intricate interactions between cosmic rays and structured magnetic turbulence, we run test-particle experiments in snapshots of a strongly turbulent magnetohydrodynamics simulation. We characterise particle–turbulence interactions via the gyro radii of particles and their experienced field-line curvatures, which reveals two distinct transport modes: magnetised motion, where particles are tightly bound to strong coherent flux tubes and undergo large-scale mirroring; and unmagnetised motion, characterised by chaotic scattering through weak and highly tangled regions of the magnetic field. We formulate an effective stochastic process for each mode: compound subdiffusion with long mean free paths for magnetised motion, and a Langevin process with short mean free paths for unmagnetised motion. A combined stochastic walker that alternates between these two modes accurately reproduces the mean squared displacements observed in the test-particle data. Our results emphasise the critical role of coherent magnetic structures in comprehensively understanding cosmic-ray transport and lay a foundation for developing a theory of geometry-mediated transport.

Key words: astrophysical plasmas, plasma flows, plasma simulation

1. Introduction

Turbulence inevitably appears wherever nonlinear flows are at play, which applies to virtually all astrophysical plasmas, such as the solar wind (Engelbrecht *et al*. 2022), the interstellar medium (Elmegreen & Scalo 2004) or the intracluster medium (Ryu *et al*. 2012). It plays a key role in answering questions about the physics of cosmic rays, such as those regarding transport and energisation processes, as well as

the effects of self-generated turbulence and dynamically relevant pressure (Amato & Blasi 2018). Applications, including those reported by Hopkins *et al*. (2020), Dörner *et al*. (2023), Ewart *et al*. (2024) and Kamal Youssef & Grenier (2024), rely on a solid understanding of the transport of fast charged particles through turbulent magnetic fields, which has been intensively studied since the work of Parker (1965). However, due to the highly complex nature of plasma turbulence and the strong dependence of cosmic-ray transport on turbulence properties, a comprehensive description is difficult to attain. This is illustrated by the circumstance that, despite extensive work, existing phenomenological theories are hardly compatible with the available observed cosmic-ray data, as recently discussed by Hopkins *et al*. (2022) and Kempski & Quataert (2022).

In large parts of the existing literature, the principal paradigm in understanding the interplay between cosmic rays and magnetic turbulence has been gyro-resonance, i.e. scattering of particles by Alfvén waves for comparable gyro radii and wavenumbers (Kulsrud 2005). These waves can either be self-generated by streaming cosmic rays (Skilling 1975) or emerge as the constituting parts of an extrinsic turbulent cascade. The latter case is classically treated with quasi-linear theory (QLT), where small-angle scattering in pitch angle caused by gyro-resonance accumulates to a random walk of the particle along a magnetic field line (Jokipii 1966; Mertsch 2020; Reichherzer *et al*. 2020; Els *et al*. 2024). However, this paradigm views magnetic turbulence merely as an ensemble of linear space-filling magnetohydrodynamic (MHD) waves with a given energy spectrum. This is incompatible with strong MHD turbulence (Meyrand, Galtier & Kiyani 2016), which tends to form coherent structures, i.e. ordered patches characterised by strong alignment and reduced nonlinearity (see, e.g. Perez & Boldyrev 2009; Matthaeus *et al*. 2015). A geometric perspective on magnetic turbulence is also advocated by, e.g. Grauer, Krug & Marliani (1994), Politano & Pouquet (1995), Grauer & Marliani (2000), Boldyrev (2006), Mininni, Pouquet & Montgomery (2006) and Malara, Perri & Zimbardo (2021). Coherent structures have been extensively observed in the solar wind (Tu & Marsch 1995; Khabarova *et al*. 2021; Vinogradov *et al*. 2024) and numerically studied in the context of cosmic-ray acceleration (Arzner *et al*. 2006; Lemoine 2021; Pezzi, Blasi & Matthaeus 2022; Pugliese *et al*. 2023).

While strong turbulence as a mixture of coherent and chaotic structures marginally reproduces the expected energy spectrum, such an averaging argument does not readily apply to cosmic-ray transport, because the transport coefficients depend strongly on the geometry and distribution of these structures. This was demonstrated by Shukurov *et al*. (2017), who found longer mean free paths (MFPs) of test particles in a fluctuating dynamo compared with random-phase synthetic turbulence with the same energy spectrum. Additionally, coherent structures may act as non-resonant magnetic mirrors (Chandran *et al*. 1999; Albright *et al*. 2001; Bell *et al*. 2025) and govern field-line wandering, which are two important mechanisms observed in test-particle experiments in snapshots of MHD simulations (Beresnyak, Yan & Lazarian 2011; Xu & Yan 2013; Cohet & Marcowith 2016; Zhang & Xu 2024). The wandering of field lines is also important for the effective diffusion of streaming cosmic rays (Sampson *et al*. 2023). Further, sharply curved magnetic field lines, which may arise at the interfaces between coherent structures, were recently invoked as an effective scattering agent for cross-field transport (Kempski *et al*. 2023; Lemoine 2023). Even though a micro-physical theory of cosmic-ray transport beyond gyro-resonance is not yet available, the general understanding of magnetic turbulence has improved significantly in recent years (see Schekochihin 2022 for a comprehensive review),

thus providing the foundations for the development of such a theory. That is not to say that gyro-resonance is entirely obsolete; rather, actual transport behaviour likely results from the interplay of several different mechanisms with varying contributions, depending on the turbulent properties of a given astrophysical system, which may vary in space and scale.

In this paper, we explore how a theory of cosmic-ray transport mediated by turbulence-induced geometry may look like. We do this by means of test-particle experiments in an MHD simulation of a fluctuating dynamo, where a dynamically dominant flow amplifies an initially small magnetic field and produces pronounced coherent flux tubes (Schekochihin *et al*. 2004; Rincon 2019; Seta *et al*. 2020). This process is believed to play an important role in the generation of magnetic fields in galaxies (Rieder & Teyssier 2017; Gent *et al*. 2024) and the intracluster medium (Vazza *et al*. 2018; Steinwandel *et al*. 2024), with initial seed fields possibly provided by the Weibel instability (Sironi, Comisso & Golant 2023; Zhou *et al*. 2024). To understand the connection between test-particle motion and magnetic field geometry, we investigate magnetic moment variations and mean squared displacements (MSDs) conditional on the gyro radii of the particles and their experienced field-line curvature. This reveals two distinct modes of transport, namely magnetised motion, where particles are closely bound to a strong and ordered magnetic field inside coherent structures, and unmagnetised motion consisting of chaotic scattering through a weak and tangled magnetic field. This description can be made more precise by fitting a stochastic model to the test-particle motion, where field-line wandering and mirroring in the magnetised case are represented by compound subdiffusion (Balescu, Wang & Misguich 1994; Qin, Matthaeus & Bieber 2002; Neuer & Spatschek 2006; Minnie *et al*. 2009), and the chaotic scattering in the unmagnetised case is represented by a three-dimensional (3-D) Langevin equation (Chandrasekhar 1943; Bian & Li 2024). We conclude our treatment by discussing implications and open questions towards a proper theory for cosmic-ray transport.

The paper proceeds by presenting the MHD simulation and test-particle experiments in § 2, followed by the stochastic model and fitting procedure in § 3. We then discuss the implications of our results in § 4, and conclude with an outlook in § 5 and a summary in § 6.

2. MHD and test-particle simulations

2.1. *MHD simulation set-up*

We perform a simulation of incompressible visco-resistive MHD turbulence in a 3-D periodic box. The governing equations of the flow field $\boldsymbol{u}$ and the magnetic field $\boldsymbol{B}$, which are given by (Biskamp 2003)

$$\frac{\partial \boldsymbol{u}}{\partial t} + \boldsymbol{u}\cdot\boldsymbol{\nabla}\boldsymbol{u} = \boldsymbol{B}\cdot\boldsymbol{\nabla}\boldsymbol{B} - \boldsymbol{\nabla} p - \nu_h(-\Delta)^h\boldsymbol{u} + \boldsymbol{f}, \quad \boldsymbol{\nabla}\cdot\boldsymbol{u} = 0, \tag{2.1a}$$

$$\frac{\partial \boldsymbol{B}}{\partial t} + \boldsymbol{u}\cdot\boldsymbol{\nabla}\boldsymbol{B} - \boldsymbol{B}\cdot\boldsymbol{\nabla}\boldsymbol{u} = -\eta_h(-\Delta)^h\boldsymbol{B}, \quad \boldsymbol{\nabla}\cdot\boldsymbol{B} = 0, \tag{2.1b}$$

with hyper-viscosity ν_h and hyper-resistivity η_h of order h, are solved with our pseudo-spectral code *SpecDyn* (Wilbert, Giesecke & Grauer 2022; Wilbert 2023). The equations are solved on a 3-D uniform grid with 1024^3 points and periodic boundary conditions. The length of the domain is $L_{\mathrm{box}} = 2\pi$ and the time scale of the flow is $T_{\mathrm{eddy}} = L_{\mathrm{box}}/u_{\mathrm{rms}}$. We set $\nu_h = \eta_h$, resulting in the magnetic Prandtl number $Pr_m = 1$. The magnetic field $\boldsymbol{B}$, which is specified in Alfvénic units $[B] = [u]$, is

h	$\boldsymbol{w}$	ν_h, η_h	ν_{eff}, η_{eff}	w_{rms}	$Re_{w,T}$
1	$\boldsymbol{u}$	1.2×10^{-3}	1.2×10^{-3}	2.423	433.463
1	$\boldsymbol{B}$	1.2×10^{-3}	1.2×10^{-3}	1.415	94.379
2	$\boldsymbol{u}$	3.6×10^{-8}	6.2×10^{-4}	2.868	493.659
2	$\boldsymbol{B}$	3.6×10^{-8}	5.4×10^{-4}	2.079	217.751

TABLE 1. MHD simulation parameters, for grid size 1024^3, box length $L_{\text{box}} = 2\pi$ and fields $\boldsymbol{w} \in \{\boldsymbol{u}, \boldsymbol{B}\}$. The maximal resolved de-aliased wavenumber is $k_{\text{max}} = 341$. The Reynolds numbers are based on the Taylor scale $k_{w,T}$ reported in table 2, and for $h = 2$, on the effective viscosity ν_{eff} and effective resistivity η_{eff} (Haugen & Brandenburg 2004).

h	$\boldsymbol{w}$	$k_{w,\text{corr}}$	$k_{w,T}$	$k_{w,\text{diss}}$	$k_{\parallel}$	$k_{\boldsymbol{B}\times\boldsymbol{j}}$	$k_{\boldsymbol{B}\cdot\boldsymbol{j}}$
1	$\boldsymbol{u}$	1.868	4.658	190.86	–	–	–
1	$\boldsymbol{B}$	7.811	12.492	238.822	1.777	15.04	11.769
2	$\boldsymbol{u}$	2.139	9.37	409.148	–	–	–
2	$\boldsymbol{B}$	8.983	17.682	511.787	3.233	20.499	18.142

TABLE 2. Characteristic length scales of the simulations. We report the correlation scale $k_{w,\text{corr}}$, Taylor scale $k_{w,T}$ and Kolmogorov dissipation scale $k_{w,\text{diss}}$ for both fields $\boldsymbol{w} \in \{\boldsymbol{u}, \boldsymbol{B}\}$. Additionally, we show for the magnetic field, the characteristic parallel scale $k_{\parallel}$, reversal scale $k_{\boldsymbol{B}\times\boldsymbol{j}}$ and perpendicular scale $k_{\boldsymbol{B}\cdot\boldsymbol{j}}$ (see Schekochihin *et al.* 2004).

initialised with a small-amplitude seed field with zero magnetic helicity and zero net magnetic flux. The flow field $\boldsymbol{u}$ is driven by a large-scale force density $\boldsymbol{f}$, operating on the wavenumber band $1 \leqslant k \leqslant 2$, with random amplitudes, which are δ-correlated in time to ensure constant power injection. The force density is constructed such that the injected net cross-helicity is zero (Alvelius 1999). Due to the chosen wavenumber band of the forcing, the box contains only one flow correlation cell. We run the simulations until the magnetic energy has been amplified to a statistically saturated state, and then record eight snapshots of $\boldsymbol{u}(\boldsymbol{x})$ and $\boldsymbol{B}(\boldsymbol{x})$ separated in time by T_{eddy}.

We simulate (2.1) with $h = 1$ as the baseline case and with $h = 2$ as the production case. The parameters of the simulations are listed in table 1. Setting $h = 2$ results in a sharper dissipative cut-off and, thus, an extended inertial range, which is reflected by the Reynolds numbers listed in table 1. Differences in the spectra and geometry are further reflected by the characteristic scales listed in table 2. For $h = 2$, the magnetic energy saturates at a higher level compared with $h = 1$ (see also Brandenburg & Sarson 2002); however, this does not matter for our test particle simulations, because we normalise the magnetic field to unit root-mean-square (r.m.s.) strength. Despite differences in the flux rope geometries, as indicated in table 2, we do not observe significant differences in our conditional particle statistics. Thus, subsequently, we only show the results for the case $h = 2$, which additionally allows for the meaningful inclusion of lower-energy particles due to the shorter dissipation scale.

See also § 2.3 for additional discussion of the geometric length scales.

System	$B_{\rm rms}$	$L_{\rm corr}$	r_g	E
Solar wind	5 nT[(2)]	0.01 au[(1)]	$(24.5, \ldots, 6.14) \times 10^{-5}$ au	(0.645, . . . , 0.041) MeV
Molecular clouds	1 nT[(4)]	16 mpc[(3)]	(0.393, . . . , 0.0982) mpc	(2.31, . . . , 0.577) TeV
Interstellar medium	0.1 nT[(5)]	100 pc[(6)]	(2.45, . . . , 0.614) pc	(1.45, . . . , 0.361) PeV
Intracluster medium	0.5 nT[(7)]	10 kpc[(6)]	(0.245, . . . , 0.0614) kpc	(0.723, . . . , 0.181) EeV

TABLE 3. Cosmic-ray protons affected by our considerations with $\hat{\omega}_g = 64, \ldots, 256$, characterised by the r.m.s. field strength $B_{\rm rms}$ and turbulence correlation scale $L_{\rm corr} \sim L_{\rm box}$ with values taken from: (1) Weygand *et al.* (2011); (2) Weygand *et al.* (2013); (3) Houde *et al.* (2009); (4) Crutcher (2012);, (5) Jansson & Farrar (2012); (6) Seta *et al.* (2020); and (7) Domínguez Fernández (2020). Note that values found in the literature tend to be widely spread due to the heterogeneous nature of astrophysical environments, as well as due to intrinsic observational uncertainties. The listed values serve merely as order-of-magnitude estimates. Also note that our fluctuating dynamo turbulence is not applicable to the anisotropic solar wind (Chen *et al.* 2020; Wang *et al.* 2024) and that the reported particle energies are non-relativistic with $V_0 = (0.037, \ldots, 0.009)\, c$. For these reasons, the solar wind values are shown only for reference.

2.2. *Test particle set-up*

We then study the motion of cosmic rays in these static snapshots by integrating the Newton–Lorentz equations (see Appendix A)

$$\dot{\boldsymbol{X}}_t = \boldsymbol{V}_t, \quad \dot{\boldsymbol{V}}_t = \hat{\omega}_g \boldsymbol{V}_t \times \boldsymbol{B}(\boldsymbol{X}_t) \tag{2.2}$$

with the volume-preserving Boris scheme (Boris & Shanny 1971; Ripperda *et al.* 2018). This test-particle approach is justified by assuming that relativistic cosmic rays with $V \approx c$ move in front of a non-relativistic plasma background with $u_{\rm rms} \ll c$, such that the time scales of the MHD and test particle simulations are well separated, i.e. $T_{\rm particle} \ll T_{\rm eddy}$ with $T_{\rm particle} = L_{\rm box}/V_0$. We can then neglect the influence of the electric field, implying conservation of energy for our test particles. The particles are parametrised by the normalised r.m.s. gyro frequency

$$\hat{\omega}_g = \frac{q B_{\rm rms}}{\gamma m} \frac{L_{\rm box}}{V_0}, \tag{2.3}$$

which includes the amplitudes V_0 of the particle velocity and $B_{\rm rms}$ of the magnetic field; (2.2) is accordingly normalised to $\|\boldsymbol{V}\| = 1$ and $B_{\rm rms} = \langle \|\boldsymbol{B}\|^2 \rangle^{1/2} = 1$. The parameter $\hat{\omega}_g$ denotes how strongly particles are coupled to the magnetic field and inversely encodes their energy via $E = \gamma m c^2 = q B_{\rm rms} L_{\rm box} c/\hat{\omega}_g$, with $V_0 = c$. Table 3 provides a mapping to specific astrophysical systems, based on typical values of the magnetic field strengths and turbulence correlation scales. Due to limited numerical resolution and the requirement to constrain the particle gyro radii to the range of resolved turbulent fluctuations, the representable particle energies are very high for the respective physical systems. How our findings extend to lower energies, such as galactic GeV protons, can only be speculated about, as we attempt in § 4.1.

The typical gyro period is given by $T_g = 2\pi\, \hat{\omega}_g^{-1}$ and we employ a fixed time step $\Delta t = 10^{-2}\, T_g$ for the integration of (2.2). The r.m.s. and instantaneous normalised gyro radii are respectively estimated by $\langle \hat{r}_g \rangle = (\pi/2)\hat{\omega}_g^{-1}$ and $\hat{r}_{g,t} = \sqrt{1-\mu_t^2}\, \hat{\omega}_g^{-1} B^{-1}(\boldsymbol{X}_t)$, where $\mu_t = \hat{\boldsymbol{V}}_t \cdot \hat{\boldsymbol{B}}(\boldsymbol{X}_t)$ denotes the pitch angle cosine. We

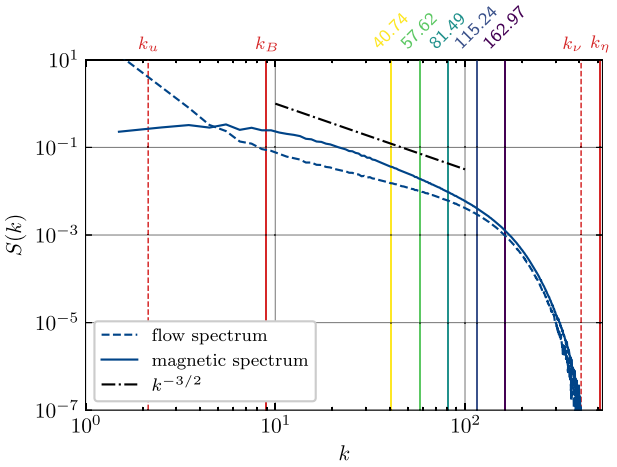

FIGURE 1. Radially averaged power spectra of flow and magnetic field in the statistically saturated state of the simulation with $h = 2$. Indicated are the wavenumbers of the integral scales $k_u = 2.139$ and $k_B = 8.983$, the effective Kolmogorov dissipation scales $k_\nu = 409.148$ and $k_\eta = 511.787$, as well as the r.m.s. gyro wavenumbers $(\pi/2)^{-1}\hat{\omega}_g$ of the considered gyro frequencies $\hat{\omega}_g = 64$; 90.51; 128; 181.019; 256.

select five values between $\hat{\omega}_g = 256$ and $\hat{\omega}_g = 64$, where particles with larger values follow field lines more closely, whereas particles with smaller values average magnetic structures more coarsely and exhibit behaviour akin to a random walk. The respective gyro scales $\langle \hat{r}_g \rangle^{-1}$ are shown in figure 1 in relation to the radially averaged energy spectra of the flow and magnetic field.

We solve (2.2) with our *ParticlePusher* code, which is able to record binned statistics of arbitrary quantities along particle trajectories. We use the local gyro average of a quantity Q along a particle trajectory $\boldsymbol{X}_t$, which is defined as

$$\bar{Q}(\boldsymbol{X}_t) = \frac{1}{\tilde{T}_g(\boldsymbol{X}_t)} \int_0^{\tilde{T}_g(\boldsymbol{X}_t)} Q(\boldsymbol{X}_{t-t'})\,\mathrm{d}t', \tag{2.4}$$

where the local gyro period is estimated as $\tilde{T}_g(\boldsymbol{X}_t) = 2\pi(\hat{\omega}_g \int_0^{T_g} B(\boldsymbol{X}_{t-t'})\,\mathrm{d}t'/T_g)^{-1}$. In the magnetised limit $r_g \ll B/\nabla B$, particles coherently gyrate along an ordered field and $\bar{Q}$ describes the well-defined gyro-centre motion, while in the unmagnetised limit $r_g \gg B/\nabla B$, particles exhibit highly chaotic motion and $\bar{Q}$ quantifies the competition between the particle's inertia and the quickly varying Lorentz force. Analogously, we define the local gyro variance as

$$\delta\overline{Q}^2(\boldsymbol{X}_t) = \overline{\left(Q(\boldsymbol{X}_t) - \bar{Q}(\boldsymbol{X}_t)\right)^2}. \tag{2.5}$$

To investigate scattering and transport behaviour of particles in the magnetised and unmagnetised regimes, we consult the geometric picture of Lemoine (2023) and Kempski *et al*. (2023) based on the field-line curvature

$$\kappa = \frac{\|\boldsymbol{B}/B \times (\boldsymbol{B}\cdot\nabla\boldsymbol{B})\|}{B^2}, \tag{2.6}$$

where $\kappa r_g \ll 1$ corresponds to the magnetised case, $\kappa r_g \gg 1$ corresponds to the unmagnetised case and for $\kappa r_g \sim 1$ order-unity variations of the magnetic moment,

$$M = \frac{\gamma m V_\perp^2}{2B} = \frac{\gamma m \left(1-\mu^2\right)}{2B} \tag{2.7}$$

are expected. Based on these definitions, we record the average of the relative variation of the magnetic moment conditional on the field-line curvature and particle gyro radius,

$$\left\langle \frac{\overline{\delta M}}{\overline{M}} \middle| \bar{\kappa}, \bar{r}_g \right\rangle. \tag{2.8}$$

Further, we record spatial mean squared displacements (MSDs) of particles

$$\langle \Delta X_\tau^2 \mid \text{cond.} \rangle = \langle \| \boldsymbol{X}_{t+\tau} - \boldsymbol{X}_t \|^2 \mid \text{cond.} \rangle, \tag{2.9}$$

conditional on the magnetisation criteria $\bar{\kappa}\bar{r}_g < 1$ and $\bar{\kappa}\bar{r}_g > 1$, as well as an unconditional baseline. We assume stationarity $\langle \| \boldsymbol{X}_\tau - \boldsymbol{X}_0 \|^2 \rangle = \langle \| \boldsymbol{X}_{t+\tau} - \boldsymbol{X}_t \|^2 \rangle$, expressed by the local time scale τ. The MSD, obtained from the displacement of individual particles, measures the time-dependent spread of the underlying particle distribution function, and classifies the motion as super-, normal or sub-diffusive, depending on $\langle \Delta X_\tau^2 \rangle \sim \tau^\alpha$ scaling with $\alpha > 1$, $= 1$ or < 1. For $\alpha = 1$, the classical diffusion coefficient is given by $D_\infty = \lim_{\tau\to\infty} \langle \Delta X_\tau^2 \rangle / 2\tau$ (Metzler & Klafter 2000).

The unconditional MSD should be treated with care, because it averages over many different length scales, thus hiding relevant physical processes, which we address by conditioning on the magnetisation criterion. Further, since our simulation box only contains one flow correlation cell, and the parallel scale of the magnetic field $k_\parallel$ is comparable to the box size, D_∞ converges only after particles traverse the periodic domain multiple times. In doing so, particles likely re-enter the box at a different position and thus sample different regions of the magnetic field, which results in a meaningful albeit biased value for D_∞.

To obtain the conditional statistics, we simulated for each $\hat{\omega}_g$, in each of the eight statistically independent MHD snapshots, 400 000 independent test-particle trajectories for 1000 gyro periods. The unconditional baseline MSD is, per snapshot, based on 40 000 independent test-particle trajectories with lengths of 10 000 gyro periods. This ensures that the tails of the joint density $p(\bar{\kappa}, \bar{r}_g)$ are well resolved. However, the conditional MSD at large time scales is hard to resolve properly, even with increased sample sizes. This matter is discussed in more detail in § 3.2.

2.3. *MHD simulation results*

We start by inspecting the magnetic field snapshots extracted from the statistically saturated phase of the MHD simulation. Figure 2 shows isosurfaces of the magnetic field strength B and the current density magnitude $j = \|\boldsymbol{\nabla} \cdot \boldsymbol{B}\|$ at different zoom levels in the simulation box. The isosurfaces of B reveal characteristic structures of the saturated fluctuating dynamo (Miller 2019; Seta *et al*. 2020), which can be described as long flattened tubes with length l, width w and height h, ordered as $l \gg w > h$. As indicated in figure 4, they contain coherent bundles of field lines and approximately represent flux surfaces. Thus, henceforth, we refer to these coherent structures as flux tubes. The connection between field strength B and coherent geometry with small curvatures κ is formally expressed by the anti-correlation between the two quantities $B \sim \kappa^{-1/2}$ (Schekochihin *et al*. 2004).

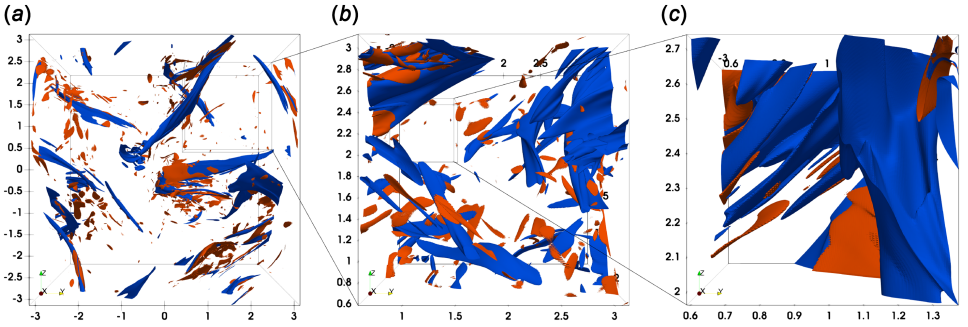

FIGURE 2. Isosurfaces of the magnetic field strength B (blue) and the current density magnitude $j = \|\boldsymbol{\nabla} \cdot \boldsymbol{B}\|$ (red). (*a*) Whole box with $B_{\mathrm{iso}}/B_{\mathrm{max}} = 0.7$ and $j_{\mathrm{iso}}/j_{\mathrm{max}} = 0.418$. (*b*) Cutout with $B_{\mathrm{iso}}/B_{\mathrm{max}} = 0.489$ and $j_{\mathrm{iso}}/j_{\mathrm{max}} = 0.303$. (*c*) Cutout with $B_{\mathrm{iso}}/B_{\mathrm{max}} = 0.245$ and $j_{\mathrm{iso}}/j_{\mathrm{max}} = 0.115$. The subscript *iso* denotes the value at which the isosurfaces are drawn. The structures of the magnetic isosurfaces correspond to flux tubes, as indicated in figure 4, which are amplified by the fluctuating dynamo action. Most of the magnetic energy is concentrated on large scales in a few intense flux tubes, while small scales reveal less intense and tightly folded flux tubes. Current sheets appear in close proximity to intense flux tubes and are embedded between folds.

At the outermost zoom level in figure 2, we recognise that most of the magnetic energy is distributed intermittently throughout the domain, concentrated in a few intense flux tubes with almost circular cross-sections, which extend up to the flow correlation scale $l \lesssim L_u$. These structures are sometimes observed wrapped up by intense current sheets. Further zooming into apparently quiet regions reveals a population of smaller, less intense, flattened flux tubes, organised in a tightly folded pattern (Schekochihin *et al*. 2004) with embedded current sheets. The networks of flux tubes and current sheets are dual to each other. Outside of coherent flux tubes, e.g. in the debris of disrupted structures, field lines tend to be chaotically tangled and highly disorganised. Additionally, reconnection (either due to resistive diffusion or due to tearing) of folded flux tubes is observed to seed small-scale plasmoids (Galishnikova, Kunz & Schekochihin 2022). This diverse picture is illustrated by a slice plot through an intense flux tube and its surroundings in figure 3.

The conventionally computed correlation wavenumber $k_{B,\mathrm{corr}}$ does not adequately reflect the geometric structure of the magnetic field, as indicated by its rather large value $O(10\,k_{\mathrm{forcing}})$, because the intermittent and highly correlated flux tubes are averaged out. It is thus instructive to also report the characteristic geometric scales $k_{\parallel}$, $k_{\boldsymbol{B}\cdot\boldsymbol{j}}$ and $k_{\boldsymbol{B}\cdot\boldsymbol{j}}$, which are sensitive to the local direction of the magnetic field (see table 2; Schekochihin *et al*. 2004; Galishnikova *et al*. 2022). For $h = 2$, these values confirm elongated tube-like structures with length $l_{\parallel} \approx L_u$ and an approximate aspect ratio of $1 : 6 : 6$. However, the flow $\boldsymbol{u}$ exhibits a lower degree of intermittency compared with $\boldsymbol{B}$, so the correlation wavenumber is more suitable to characterise its correlation structure. The small discrepancy between $k_{u,\mathrm{corr}}$ and k_{forcing} results from the presence of a broadband turbulent energy spectrum (Seta *et al*. 2020).

2.4. *Test particle results*

Figure 4 shows examples of test-particle trajectories. Particles are clearly magnetised with $\bar{\kappa}\bar{r}_g < 1$ inside the intense flux tube, where they closely follow magnetic field lines. Due to large-scale variations of the illustrated flux tube, particles undergo occasional mirroring events, which appear as sudden reversals of direction. These

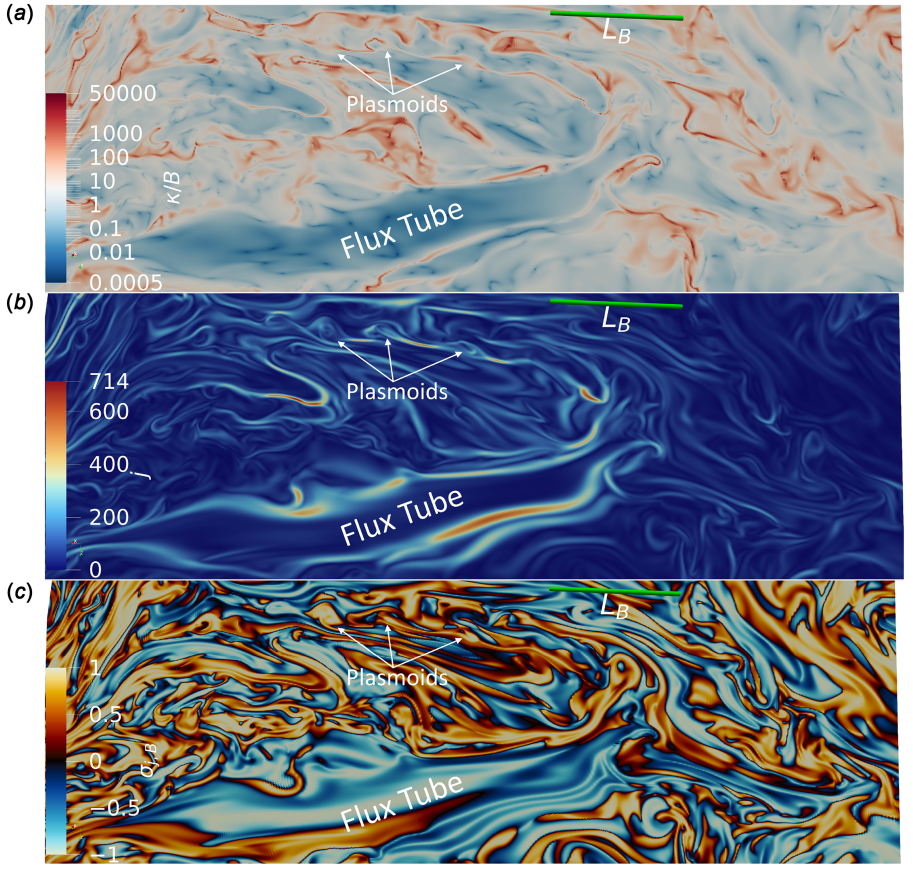

FIGURE 3. Slices through a magnetic flux tube, surrounded by tight folds, current sheets and plasmoids. (*a*) Field-line curvature divided by the field strength κ/B for comparison with the magnetisation criterion $\kappa r_g \sim 1$ with $r_g \propto B^{-1}$. (*b*) Magnitude of the current density j indicating intense current sheets. (*c*) Alignment between the magnetic field and current density $\sigma_{j,B} = \hat{\boldsymbol{j}} \cdot \hat{\boldsymbol{B}}$ indicating cellularisation into approximately force-free patches. Further indicated are the correlation scale of the magnetic field and the locations of the flux tube and example plasmoids.

rare reversals imply a long parallel MFP. Outside of the flux tube, particle motion is unmagnetised with $\bar{\kappa}\bar{r}_g > 1$ and appears much more erratic, as the particles bounce chaotically and with a short MFP through the tangled field. An additional interesting case is illustrated by the small-scale plasmoid, which appears to be an efficient device for trapping particles. However, since they appear to have a sub-dominant contribution in our statistics, and due to numerical concerns addressed in § 4.2, we focus here on the modelling of magnetised and unmagnetised motion, and leave a detailed study on the effect of plasmoids on particle transport for later work.

These observations are substantiated by the conditional statistics given by (2.8) and (2.9). First, figure 5 confirms that particles are magnetised in the sense that their magnetic moments are weakly conserved, $\overline{\delta M}/\overline{M} < 1$, when their gyro radii are smaller than the experienced field-line curvature radius, i.e. $\bar{\kappa}\bar{r}_g < 1$ (Lemoine 2023). If this condition is violated, i.e. $\bar{\kappa}\bar{r}_g > 1$, large variations of the magnetic moment are expected. Although $\bar{\kappa}\bar{r}_g = 1$ does not constitute an exact decision boundary, we

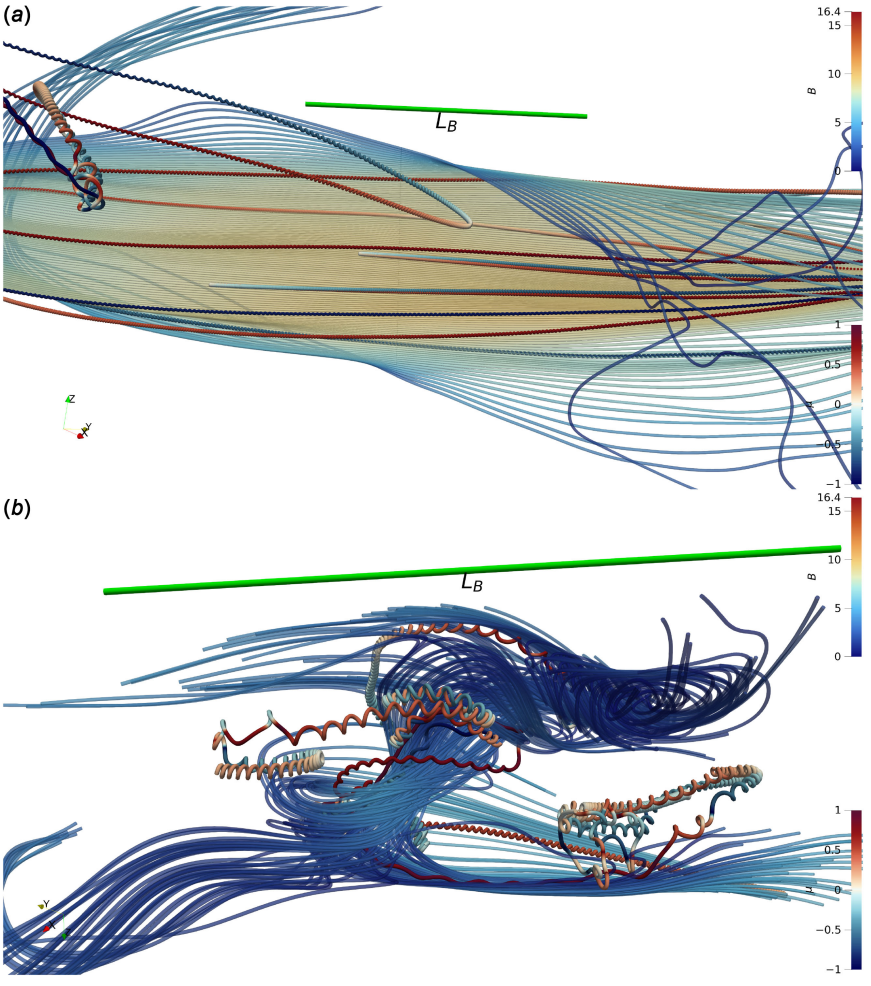

FIGURE 4. Magnetic field lines coloured by field strength B and test-particle trajectories coloured by pitch angle cosine μ in the (a) flux tube and (b) one of the plasmoids from figure 3. In the coherent flux tube, particles are closely bound to field lines with occasional large-scale mirroring. The plasmoid exhibits highly tangled field lines and effectively confines particles with a mixture of small-scale mirroring and unmagnetised scattering. The magnetic correlation scale is indicated for reference.

consider it as a useful heuristic, because our ensuing results remain qualitatively robust under minor refinements of this condition. Appendix B shows results for an alternative magnetisation criterion based on the perpendicular reversal scale $\kappa_\perp$ introduced by Kempski *et al*. (2023), which can be approximated as $\bar{\kappa}_\perp \bar{r}_g^{1/2} \sim 30$.

Second, figure 6 shows the unconditional MSD for our considered particles, as well as the conditional observations for $\hat{\omega}_g = 181.019$. The unconditional data reveal three time scales of transport: particles move ballistically on short time scales, followed by a transient subdiffusive phase, before becoming asymptotically diffusive. As noted in § 2.2, convergence to normal diffusion occurs only after the MSD reaches the box size, which means that particles may experience the same structures repeatedly due to the periodic boundary conditions. We address this issue partly by

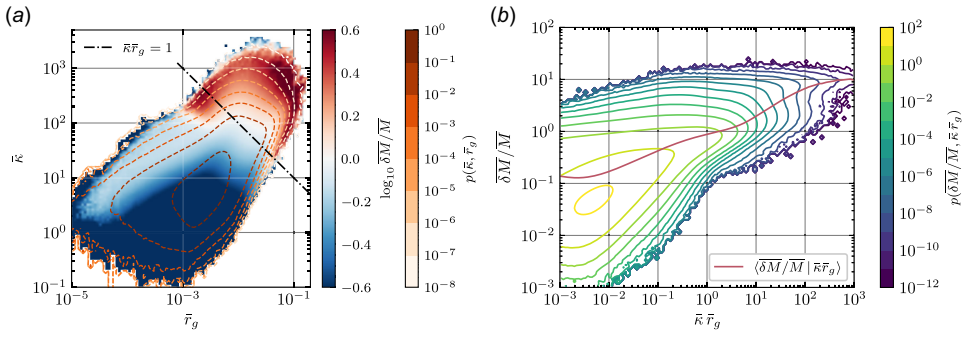

FIGURE 5. (*a*) Average of the relative magnetic moment variation $\overline{\delta M}/\overline{M}$ conditional on particle gyro radius $\bar{r}_g$ and field-line curvature $\bar{\kappa}$. All recorded quantities are gyro-averaged. The colour scale is centred at $\overline{\delta M}/\overline{M} = 1$, where particles can be considered magnetised for smaller variations and unmagnetised for larger variations. Further, the colour scale is capped to $\log_{10} \overline{\delta M}/\overline{M} \in (-0.6, 0.6)$ to highlight the transition region. This transition region is compared with the magnetisation criterion $\bar{\kappa}\bar{r}_g \sim 1$ expected from the field-line curvature picture. The joint density $p(\bar{\kappa}, \bar{r}_g)$ is indicated for reference. (*b*) Conditional average $\langle \overline{\delta M}/\overline{M} | \bar{\kappa}\bar{r}_g \rangle$ also showing the transition from predominantly magnetised and to predominantly unmagnetised motion as $\bar{\kappa}\bar{r}_g$ increases, although the joint density $p(\overline{\delta M}/\overline{M}, \bar{\kappa}\bar{r}_g)$ reveals some uncertainty of this criterion.

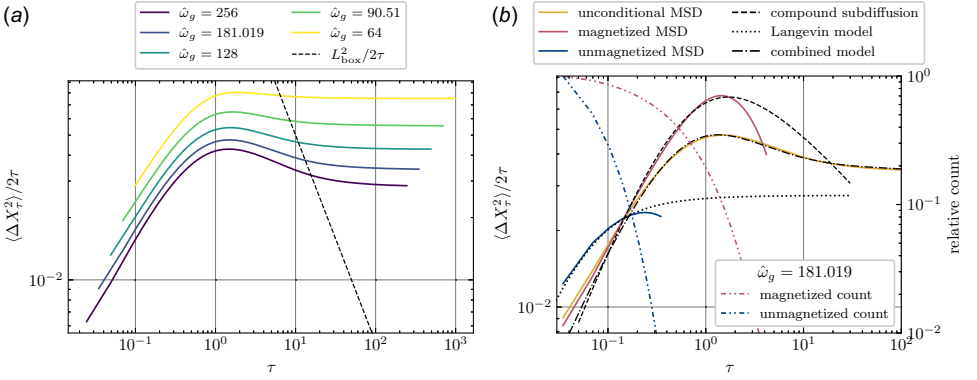

FIGURE 6. (*a*) MSD of the test particles, depending on the time lag τ, revealing initial ballistic propagation, transient subdiffusion and asymptotic diffusive behaviour. Notably, diffusion only occurs for mean square displacements beyond the simulation box size. (*b*) Conditional MSD for magnetised and unmagnetised transport for a selected test-particle energy, as well as the respective relative bin counts. Longer consecutively magnetised or unmagnetised segments have a lower probability than shorter ones, which leads to a systematically smaller sample size for the conditional averages at larger time scales τ. We describe magnetised transport by compound subdiffusion and unmagnetised transport by a Langevin equation. The discrepancy between magnetised data and model are likely due to this bias at large τ, which is addressed when tuning the combined model to the unconditional MSD, resulting in good agreement.

modelling the transport behaviour on short and intermediate time scales, where the bias of the periodic domain is negligible.

The conditional data support two distinct transport behaviours, where magnetised particles exhibit much longer MFPs compared with unmagnetised particles.

Also indicated are the relative bin counts contributing to the conditional averages. This number strongly decreases for both cases for larger time scales, because the probability of finding an uninterrupted conditional trajectory segment decreases with its desired length. The conditional averages at large time scales are thus likely dominated by a few very intense flux tubes, implying a systematic bias caused by our heuristic magnetisation criterion $\bar{\kappa}\bar{r}_g \sim 1$. Our methodology for modelling the conditional and unconditional data, as well as addressing this bias, is presented in § 3.

3. Stochastic transport model

Motivated by our previous findings, we present a simplified stochastic model for the transport of charged test particles, resulting from a competition between magnetised and unmagnetised behaviour. We assume that the magnetised behaviour is dictated by the most intense flux tubes which extend up to the correlation scale of the turbulence $\lambda_{\mathrm{fl}} \lesssim L_u$. Particles are strictly bound to those field lines, but may undergo pitch-angle scattering with rate θ_μ. This scattering represents large-scale mirror interactions on the scale of the flux tubes, and thus, its MFP $\lambda_\mu \sim c/\theta_\mu$ is expected to be long and comparable to the flux tube scale, i.e. $\lambda_\mu \sim \lambda_{\mathrm{fl}}$. Particles remain in the magnetised transport state for some mean duration t^*_μ, which represents the mean time until a scattering event due to sharp field-line curvature occurs.

However, unmagnetised behaviour results from an interplay between the intrinsic particle momentum and random scattering due to highly tangled field lines, where no well-defined mean field is seen by the particle, so we expect a relatively short MFP and high scattering rate $\theta_{\mathrm{scatter}} \sim c/\lambda_{\mathrm{scatter}}$. Particles wander around the domain for some mean duration t^*_{scatter} until they encounter a strong flux tube and become magnetised again.

For the sake of comparison, we can estimate the MFP of the unconditional asymptotic diffusion process as $\lambda_{\mathrm{asymp}} \sim D_\infty/c$ (this will be specified more precisely later), and we expect the ordering

$$\lambda_{\mathrm{scatter}} < \lambda_{\mathrm{asymp}} < \lambda_\mu \sim \lambda_{\mathrm{fl}}. \tag{3.1}$$

The mean durations parametrise escape-time probability distributions $p_\mu(t|t^*_\mu)$ and $p_{\mathrm{scatter}}(t|t^*_{\mathrm{scatter}})$ for both transport modes. They may be related to the distribution of field-line curvature, and from the dominance of low curvatures, we expect the ordering

$$t^*_{\mathrm{scatter}} < t^*_\mu. \tag{3.2}$$

We assume here that each kind of motion (specifically field-line wandering, magnetised mirroring and unmagnetised scattering) is sufficiently characterised by its respective MFP λ and thus adequately modelled by a Langevin equation, where both initial ballistic and asymptotic diffusive behaviour are resolved. The emergent combined transport behaviour can then be studied as a competition between the involved MFPs and mean durations. Further, the combination of two simple Langevin-like descriptions readily leads to compound subdiffusion and thus, a plausible explanation for the transient subdiffusion shown by the test particles. We emphasise that qualitative descriptions are linked to the relative sizes of the various MFPs, for instance, 'coherent motion' or 'large-scale mirroring' correspond to $\lambda_\mu \sim L_u$, while 'chaotic motion' corresponds to $\lambda_{\mathrm{scatter}} \ll L_u$.

3.1. *Stochastic differential equations*

We start with describing the motion of field lines and unmagnetised particles by a 3-D Langevin equation (Chandrasekhar 1943; Bian & Li 2024)

$$\mathrm{d}\boldsymbol{X}_s = \boldsymbol{V}_s\,\mathrm{d}s, \quad \mathrm{d}\boldsymbol{V}_s = -\theta\boldsymbol{V}_s\,\mathrm{d}s + \sqrt{\frac{2}{3}\theta v_{\mathrm{rms}}^2}\,\mathrm{d}\boldsymbol{W}_s, \tag{3.3}$$

where $\boldsymbol{V}_s$ and $\boldsymbol{X}_s$ denote velocity and position of the random walker at the generalised time or path parameter s. The walker is parametrised by the scattering rate θ and thermal velocity v_{rms}, and driven by 3-D Gaussian white noise $\mathrm{d}\boldsymbol{W}_s$ with the correlation function $\langle \mathrm{d}W_{i,s}\,\mathrm{d}W_{j,s'}\rangle = \delta_{ij}\delta(s-s')$. The MSD is given by (as shown in Appendix C.1)

$$\langle X_s^2\rangle = \langle \|\boldsymbol{X}_s\|^2\rangle = \frac{2v_{\mathrm{rms}}^2}{\theta^2}\left(e^{-\theta s} + \theta s - 1\right), \tag{3.4}$$

which scales asymptotically as $\langle X_s^2\rangle \underset{s\to 0}{\sim} v_{\mathrm{rms}}^2 s^2$ and $\langle X_s^2\rangle \underset{s\to\infty}{\sim} 2v_{\mathrm{rms}}^2 s/\theta$. The MFP is accordingly given by the scattering rate and thermal velocity as

$$\lambda = \frac{v_{\mathrm{rms}}}{\theta} = \frac{D_{xx}}{v_{\mathrm{rms}}}, \tag{3.5}$$

with $D_{xx} = \lim_{s\to\infty}\langle X_s^2\rangle/2s$. In the following, we set $v_{\mathrm{rms}} = 1$ for field lines and unmagnetised transport in accordance with the normalisation choices $\|\boldsymbol{V}\| = 1$ and $\langle\|\boldsymbol{B}\|^2\rangle = 1$ according to § 2.

Next, we describe pitch-angle motion of magnetised particles with an Itô stochastic differential equation of the form (Strauss & Effenberger 2017)

$$\mathrm{d}s_t = v_{\mathrm{eff}}\mu_t\,\mathrm{d}t, \quad \mathrm{d}\mu_t = \frac{\mathrm{d}D_{\mu\mu}(\mu_t)}{\mathrm{d}\mu}\,\mathrm{d}t + \sqrt{2D_{\mu\mu}(\mu_t)}\,\mathrm{d}W_t, \tag{3.6}$$

where s_t denotes the displacement along a field line at time t and $\mu_t \in (-1, 1)$, with reflective boundary conditions, denotes the pitch angle cosine. The effective velocity v_{eff} reflects anisotropies of the pitch-angle-cosine distribution, where $v_{\mathrm{eff}} = 1$ indicates an isotropic uniform distribution. The process is driven by uncorrelated Gaussian white noise with $\langle \mathrm{d}W_t\,\mathrm{d}W_{t'}\rangle = \delta(t-t')$ and is characterised by the pitch angle diffusion coefficient

$$D_{\mu\mu}(\mu) = D_0\left(1-\mu^2\right). \tag{3.7}$$

We choose this generic isotropic shape of $D_{\mu\mu}$ in accordance with the agnostic stance of this work towards the detailed pitch-angle physics (see also van den Berg, Els & Engelbrecht 2024). Analogously to (3.4), due to the Markovian nature of this process resulting in an exponential velocity correlation function, the MSD is given by

$$\langle s_t^2\rangle = \frac{2\lambda_\mu^2}{3}\left(e^{-\theta_\mu t} + \theta_\mu t - 1\right), \tag{3.8}$$

where the additional factor 1/3 comes from the variance of the uniform distribution $\mathcal{U}(-1, 1)$. The MFP $\lambda_\mu = v_{\mathrm{eff}}/\theta_\mu$ of this process is known from the literature (Schlickeiser 2002) as

$$\lambda_\mu = \frac{3D_{ss}}{v_{\mathrm{eff}}} = \frac{3v_{\mathrm{eff}}}{8}\int_{-1}^{+1}\frac{\left(1-\mu^2\right)^2}{D_{\mu\mu}(\mu)}\,\mathrm{d}\mu, \tag{3.9}$$

with $D_{ss} = \lim_{t\to\infty}\langle s_t^2\rangle/2t$, where the integral evaluates together with (3.7) to $\lambda_\mu = v_{\text{eff}}/2D_0$.

Further, a pitch-angle walker diffusing along a diffusing field line results in compound subdiffusion, with the MSD scaling as $t^{1/2}$. The spatial position of such a random walker is found by evaluating the field-line trajectory $\boldsymbol{X}_{\text{fl},s}$, given by (3.3), at the pitch-angle displacement coordinate s_t, given by (3.6), as

$$\boldsymbol{Y}_t = \boldsymbol{X}_{\text{fl},s_t}. \tag{3.10}$$

This approach resembles Brownian yet non-Gaussian diffusion via subordination as presented by Chechkin *et al*. (2017), and guided by their techniques, we can write the MSD as the integral

$$\langle Y_t^2\rangle = \int_{-\infty}^{+\infty} \langle X_{\text{fl},|s|}^2\rangle \frac{1}{\sqrt{2\pi\,\langle s_t^2\rangle}} \exp\left(-\frac{s^2}{2\langle s_t^2\rangle}\right) \mathrm{d}s, \tag{3.11}$$

where the MSD of the field line $\langle X_{\text{fl},s}^2\rangle$ is given by (3.4) and the MSD of the pitch-angle walker $\langle s_t^2\rangle$ is given by (3.8). For the purpose of fitting (3.11) to the data, we evaluate the integral numerically with an adaptive Gaussian quadrature rule; however, the asymptotic behaviour can be written explicitly as $\langle Y_{s_t}^2\rangle \underset{t\to 0}{\sim} v_{\text{eff}}^2 t^2/3$ and $\langle Y_{s_t}^2\rangle \underset{t\to\infty}{\sim} 4\lambda_{\text{fl}}\sqrt{v_{\text{eff}}\lambda_\mu}\,t/3$, as shown in Appendix C.2.

Based on these building blocks, we construct the combined stochastic model $\boldsymbol{Z}_{\text{model},t}$. A stochastic walker alternates between magnetised and unmagnetised transport behaviour, where the duration for each segment is sampled from the respective escape-time probability distributions $p(t|t_\mu^*)$ and $p(t|t_{\text{scatter}}^*)$. For magnetised transport, we simulate a field line $\boldsymbol{X}_{\text{fl},s}$ according to (3.3) and let the walker diffuse with s_t along this field line according to (3.6). This behaviour is parametrised by the field-line and mirror MFPs λ_{fl} and λ_μ, the effective velocity v_{eff}, and the magnetised mean duration t_μ^*. Note that we simulate a new independent field line for every time the walker enters magnetised behaviour. For unmagnetised transport, we simply simulate random scattering $\boldsymbol{X}_{\text{scatter},t}$ according to (3.3), which is parametrised by the scattering MFP λ_{scatter} and the scattering mean duration t_{scatter}^*. The procedure is summarised in Algorithm 1.

3.2. *Fitting the model*

As noted in § 2.4, finding connected segments of particle trajectories, which satisfy the desired conditions $\bar{\kappa}\bar{r}_g \lessgtr 1$, becomes more difficult with increasing length of these segments. The reason for this is partly physical due to the distribution of field-line curvature, and partly methodical due to our magnetisation condition $\bar{\kappa}\bar{r}_g \sim 1$ being merely a heuristic. Thus, the conditional data $\langle \Delta X_\tau^2 | \bar{\kappa}\bar{r}_g \lessgtr 1\rangle$ come with the caveat that data points at larger time scales τ are backed by a much smaller sample size compared with data points at smaller τ. This is illustrated by the relative bin counts in figure 6(*b*). When fitting our models, we address this issue by truncating the data at a cut-off time scale τ_{cutoff}, where the choice of τ_{cutoff} should be small enough for sufficient statistical significance and large enough to provide a meaningful fit result. For the magnetised case, we choose $\tau_{\text{cutoff}} = 1.5\tau_{\text{peak}}$ with $\tau_{\text{peak}} = \text{argmax}_\tau \langle \Delta X_\tau^2 | \bar{\kappa}\bar{r}_g < 1\rangle/2t$ and ensure a minimum relative bin count of 1%. Analogously for the unmagnetised case, we choose $\tau_{\text{cutoff}} = 1\tau_{\text{peak}}$ with

Algorithm 1 Combined stochastic model

Require: number of steps n

Choose initial magnetisation $m \in \{0, 1\}$ ▷ 0: magnetised, 1: unmagnetised
Let $\boldsymbol{Z}_{\mathrm{res}} \leftarrow [\boldsymbol{0}]$
while $\mathrm{LEN}(\boldsymbol{Z}_{\mathrm{res}}) < n$ **do**
  if $m = 0$ **then**
    Sample $t' \sim p(t|t^*_\mu)$
    Simulate $s_t \leftarrow \mu - \mathrm{PROCESS}(0, t')$ ▷ (3.6) with λ_μ
    Simulate $\boldsymbol{X}_{\mathrm{fl},s} \leftarrow \mathrm{FIELDLINE{-}PROCESS}(\mathrm{MIN}(s_t), \mathrm{MAX}(s_t))$ ▷ (3.3) with λ_{fl}
    Interpolate $\boldsymbol{Y}_t \leftarrow (\boldsymbol{X}_{\mathrm{fl},s}, s_t)$ ▷ (3.10)
    Append $\boldsymbol{Z}_{\mathrm{res}} \leftarrow [\boldsymbol{Z}_{\mathrm{res}}, \boldsymbol{Y}_t]$
    Let $m \leftarrow 1$
  else if $m = 1$ **then**
    Sample $t' \sim p(t|t^*_{\mathrm{scatter}})$
    Simulate $\boldsymbol{X}_{\mathrm{scatter},t} \leftarrow \mathrm{SCATTER{-}PROCESS}(0, t')$ ▷ (3.3) with $\lambda_{\mathrm{scatter}}$
    Append $\boldsymbol{Z}_{\mathrm{res}} \leftarrow [\boldsymbol{Z}_{\mathrm{res}}, \boldsymbol{X}_{\mathrm{scatter},t}]$
    Let $m \leftarrow 0$
  end if
end while
return $\boldsymbol{Z}_{\mathrm{res}}$

$\tau_{\mathrm{peak}} = \mathrm{argmax}_\tau \langle \Delta X_\tau^2 | \bar{\kappa} \bar{r}_g > 1 \rangle / 2t$ and ensure a minimum relative bin count of 1 % as well. Despite these precautions, a systematic bias likely remains in the data, most notably in the conditional magnetised data, which is dominated at long time scales by a small number of very intense flux tubes. This remaining bias is addressed by the Bayesian optimisation of the magnetised mean duration t^*_μ and MFP λ_μ discussed later.

We proceed by fitting the compound subdiffusion model given by (3.11), which is parametrised by λ_{fl}, λ_μ and v_{eff}, to the magnetised data $\langle \Delta X_\tau^2 | \bar{\kappa} \bar{r}_g < 1 \rangle$. Since a clear distinction of the two MFPs requires reliable data at large τ, we argue that large-scale magnetic mirrors mostly operate on the correlation scale of coherent flux tubes and fix $\lambda_{\mathrm{fl}} = \lambda_\mu$, thereby reducing the number of free parameters by one. Further, we fit the Langevin model given by (3.4), which is parametrised by $\lambda_{\mathrm{scatter}}$, to the unmagnetised data $\langle \Delta X_\tau^2 | \bar{\kappa} \bar{r}_g > 1 \rangle$. We employ a nonlinear least squares method for both cases (Branch, Coleman & Li 1999). For comparison, the unconditional asymptotic MFP of the unconditional data is estimated as

$$\lambda_{\mathrm{asymp}} = \frac{D_\infty}{v_{\mathrm{rms}}} \tag{3.12}$$

with the asymptotic diffusion coefficient $D_\infty = \lim_{\tau \to \infty} \langle \Delta X_\tau^2 \rangle / 2\tau$ and the particle r.m.s. velocity $v_{\mathrm{rms}}^2 = (3/2) \lim_{\tau \to 0} \langle \Delta X_\tau^2 \rangle / \tau^2$. This choice of v_{rms} ensures consistency with the Langevin model for the unmagnetised motion. The resulting MFPs are shown in figure 7(*a*) and discussed in § 3.3. The effective pitch angle velocities v_{eff} are shown in figure 7(*b*), where $v_{\mathrm{eff}} = 1$ corresponds to an isotropic uniform pitch angle cosine distribution. We observe $v_{\mathrm{eff}} > 1$ for higher particle energies, which is likely

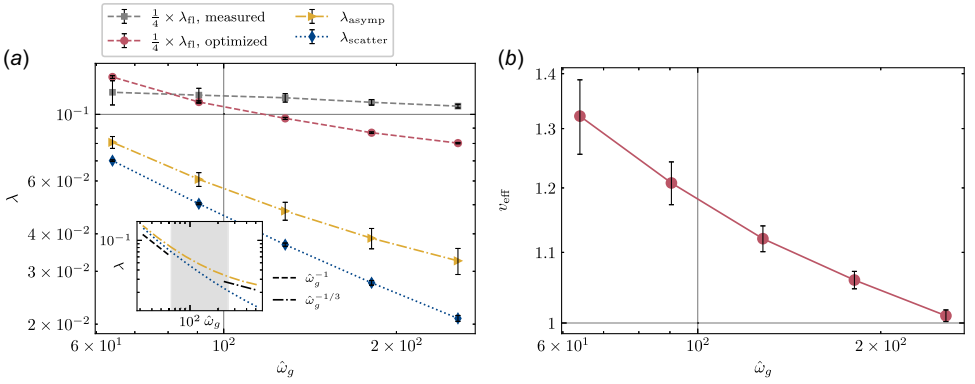

FIGURE 7. (*a*) Fitted MFPs for conditional magnetised λ_{fl} and unmagnetised transport $\lambda_{\mathrm{scatter}}$, as well as for the unconditional asymptotic case λ_{asymp}. As shown in the inset, λ_{asymp} converges to $\lambda_{\mathrm{scatter}}$ for high energies, where our magnetised model is no longer valid. Scalings $\hat{\omega}_g^{-1}$ and $\hat{\omega}_g^{-1/3}$ are indicated for reference. The field line MFP λ_{fl} is obtained twice: once by naively fitting (3.11) to the biased magnetised MSD (measured), and once by optimising the unbiased loss function given by (3.14) (optimised). Both values are scaled by a factor $1/4$ to simplify comparison with $\lambda_{\mathrm{scatter}}$ and λ_{asymp}. (*b*) Fitted effective velocity of magnetised pitch-angle diffusion. The error bars in both plots for the fitted models are given by $1.96\times$ the standard error produced by the respective fit routines. The error bars for λ_{asymp} are obtained by taking the mean and $1.96\times$ the standard deviation over the eight independent MHD snapshots.

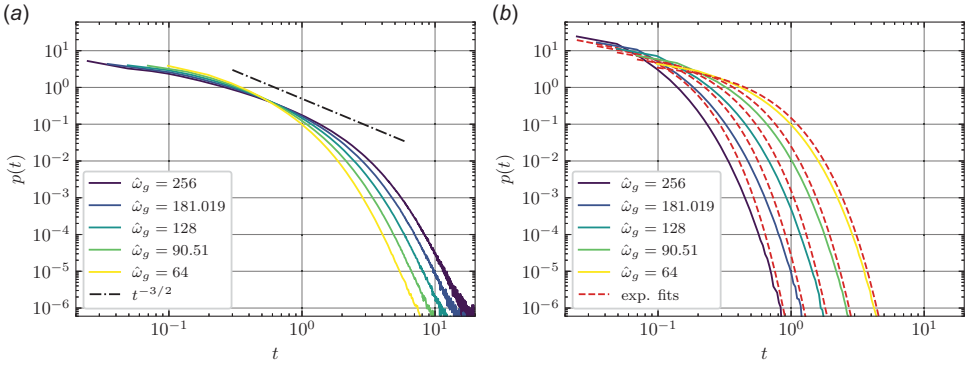

FIGURE 8. Escape-time probability distributions estimated from the conditional test-particle averages. (*a*) Magnetised cases exhibit heavier tails than an exponential distribution, indicating that the magnetised motion has some memory. The power-law scaling $t^{-3/2}$ expected for the classical first-passage time distribution of a random walker on a finite line is indicated for reference. (*b*) Unmagnetised cases closely resemble exponential distributions, indicating a memory-less Markov nature of the unmagnetised motion.

due to shorter durations of magnetised segments, thus those particles experience less mirroring, which would isotropise the pitch angles.

Next, we estimate the escape-time probability distributions by recording the lengths of observed conditional magnetised and unmagnetised segments into histograms. The densities of the histogram are plotted in figure 8, revealing an

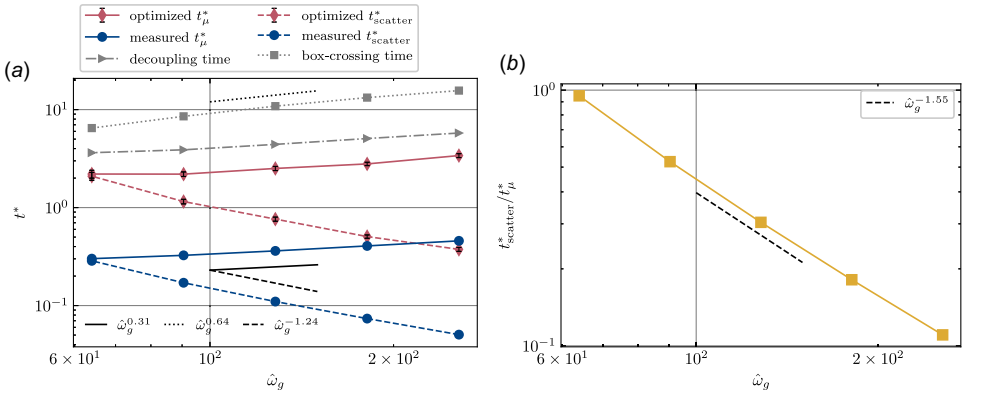

FIGURE 9. (*a*) Measured and fitted mean durations t^*_μ and t^*_{scatter}. Box-crossing and decoupling time scales are given for reference. The measured magnetised mean duration is much smaller than the expected decoupling time scale due to neglecting the correlation of large-scale flux tubes. However, the optimised mean magnetised duration is comparable to the decoupling time scale. The error bars of the optimised results are given by 1.96× the estimated confidence interval of the Bayesian optimisation procedure (see Appendix D). (*b*) Ratio of measured unmagnetised and magnetised mean durations, as a proxy for the volume filling fraction of scattering sites experienced by the test particles. The optimised mean scattering duration is determined by multiplying this measured ratio with the optimised mean magnetised duration.

exponential shape for the unmagnetised case, which corroborates the view of the unmagnetised motion as a memory-less random walk. However, the magnetised case roughly resembles a tempered power-law shape, indicating a process with long memory governed by extended flux tubes. When picturing a one-dimensional (1-D) pitch-angle walker on a field line with finite length, one would expect the classical first-passage time distribution (Krapivsky, Redner & Ben-Naim 2010), which scales as $t^{-3/2}$. This scaling is indicated for reference.

To judge whether the results are reasonable, we compare the magnetised mean duration t^*_μ with the typical box-crossing time scale τ_{box} (see figure 6*a*) and the decoupling time scale τ_{decouple}, which is estimated as the inflection point of the unconditional running diffusion coefficient $\langle \Delta X^2_\tau \rangle / 2\tau$ as

$$\tau_{\mathrm{decouple}} = \underset{\tau \in (0,\infty)}{\operatorname{argmin}} \frac{\mathrm{d} \log \langle \Delta X^2_\tau \rangle / 2\tau}{\mathrm{d} \log \tau}. \tag{3.13}$$

First, since the dominant coherent structures which govern the particle transport are comparable to the fluid correlation scale $l \lesssim L_u < L_{\mathrm{box}}$, we expect $t^*_\mu < \tau_{\mathrm{box}}$, i.e. that magnetised motion is clearly separated from the box-crossing time scale . Second, we assume that the initially ballistic and transiently subdiffusive behaviour of the unconditional MSD is given by magnetised transport, and asymptotic diffusion is linked to decoupling of particles from coherent field lines, so we expect $t^*_\mu \sim \tau_{\mathrm{decouple}}$. The various time scales are shown in figure 9(*a*), which confirms the first expectations, but reveals that the measured magnetised mean durations are shorter than expected by an order of magnitude $\tau_{\mathrm{decouple}}/t^*_\mu \sim O(10)$. Additionally, the combined model given by Algorithm 1 does not reproduce the unconditional MSD with these naively measured parameters (not shown).

This severe underestimation is likely caused by the discrepancy between our combined stochastic model, which simulates a new independent stochastic field line for each magnetised segment, and test particles in MHD snapshots, where magnetised transport is governed by a finite number of spatially correlated intense flux tubes. To explore the capabilities of our combined model, we search for an optimal effective mean magnetised duration t_μ^* by means of Bayesian optimisation (see Appendix D for details). Specifically, we minimise the loss function

$$\mathcal{L}\left(t_\mu^*, \lambda_{\mathrm{fl}}\right) = \max_{\tau \in (0, \tau_{\max})} \left| \log \frac{\langle \Delta X_\tau^2 \rangle}{\left\langle Z_{\mathrm{model},\tau}^2 | t_\mu^*, \lambda_{\mathrm{fl}} \right\rangle} \right|, \tag{3.14}$$

which compares the unconditional MSD of test particles $\langle \Delta X_\tau^2 \rangle$ with the MSD of our combined model $\langle Z_{\mathrm{model},\tau}^2 | t_\mu^*, \lambda_{\mathrm{fl}} \rangle$. We also take the field line MFP λ_{fl} as a tuneable parameter to account for the previously discussed bias of the magnetised data. Further, the effective pitch-angle walker velocity v_{eff} and scattering MFP $\lambda_{\mathrm{scatter}}$ are taken from the conditional fit results, the pitch angle MFP is fixed as $\lambda_\mu = \lambda_{\mathrm{fl}}$, and the unmagnetised mean duration is determined from the fixed measured ratio $t_{\mathrm{scatter}}^*/t_\mu^*$ (see figure 9*b*), which serves as a proxy for the volume filling fraction of scattering sites.

3.3. *Model results*

The MSDs of the combined model for the optimised values are plotted in figure 10 and agree well with the unconditional test-particle MSD for all considered particle energies. Note that the optimised magnetised mean durations are now comparable to the decoupling time scale, as shown in figure 9(*a*). Also plotted in figure 10 are the conditional MSDs and models, showing good agreement of the simple Langevin diffusion with the unmagnetised data, as well as some disagreement for the compound subdiffusion and the biased magnetised data. Specifically, as shown in figure 7(*a*), the optimisation procedure predicts for most particle energies smaller MFPs compared with the conditional data. These smaller values can account for transport by less intense flux tubes or constellations of strongly correlated flux tubes and, thus, correct the bias from the conditional magnetised data, dominated by isolated (intrinsic to the measurement methodology) and very intense flux tubes (fulfilling the heuristic magnetisation criterion for long time scales).

4. Discussion

4.1. *Implications on cosmic-ray transport*

We emphasise that the considered regime of particle energies is non-asymptotic and limited by the available numerical resolution of the MHD simulation. However, in our results, consisting of MFPs in figure 7(*a*) and mean durations in figure 9(a), tendencies towards the asymptotic high- and low-energy regimes can be recognised. On one hand, the high-energy regime with $\hat{\omega}_g \lesssim 1$ will be entirely governed by unmagnetised motion, because particles with gyro radii $r_g \gtrsim L_u$ average out any non-trivial structures, as shown by increasing $t_{\mathrm{scatter}}^*/t_\mu^*$ and $\lambda_{\mathrm{asymp}}/\lambda_{\mathrm{scatter}} \to 1$ as $\hat{\omega}_g$ decreases. The expected random-walk scaling is $\lambda \sim \hat{\omega}_g^{-2}$ (Reichherzer *et al*. 2020; the indicated scaling $\lambda \sim \hat{\omega}_g^{-1}$ in figure 7(*a*) is only transitional, compare also Lübke *et al*. 2024). The conditional magnetised model is valid to roughly $\hat{\omega}_g \sim 64$.

On the other hand, the low-energy regime $\hat{\omega}_g \gg 1$ becomes increasingly more dominated by magnetised motion as indicated by decreasing $t_{\mathrm{scatter}}^*/t_\mu^*$. The asymptotic

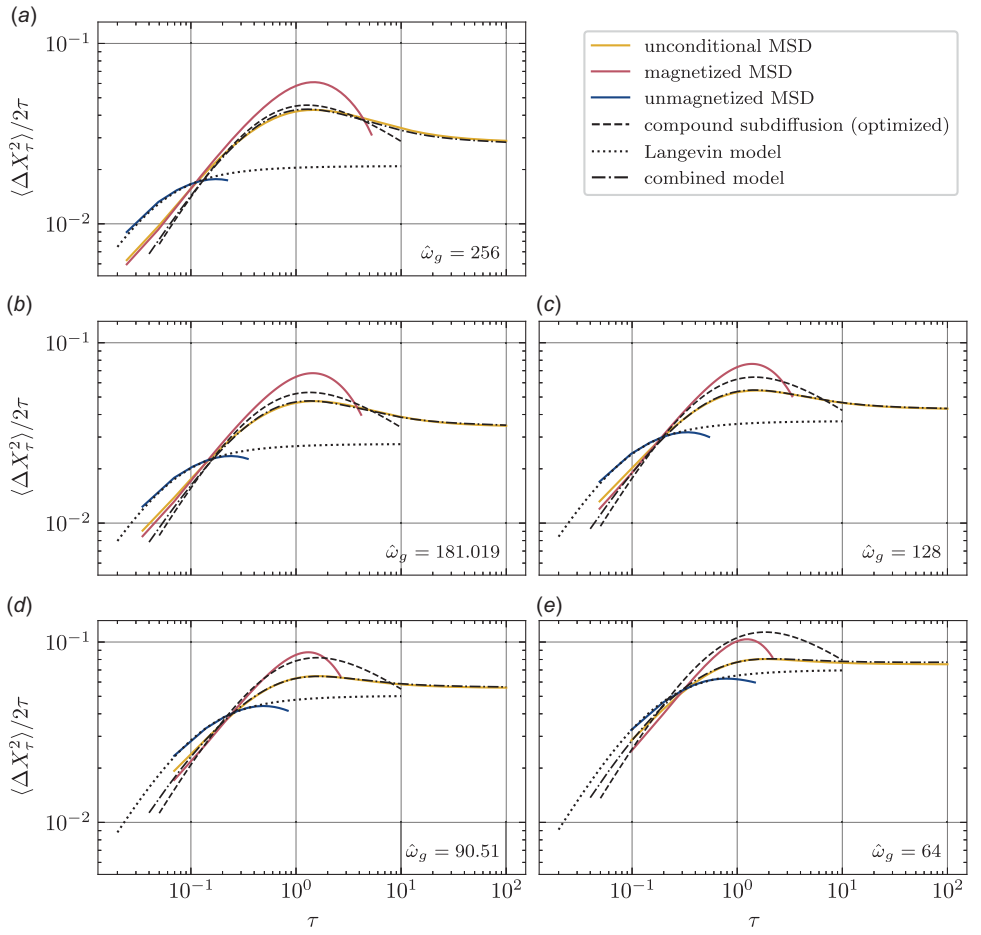

FIGURE 10. Time-dependent MSDs for conditional and unconditional test-particle measurements, as well as conditional and combined model results. The combined model with optimised parameters shows good agreement with the unconditional test-particle MSD. The compound subdiffusion model is also shown for the unbiased optimised parameters, thus some deviation from the biased conditional data is present.

MFP λ_{asymp} likely becomes a function of the coherent field line MFP λ_{fl} and the large-scale mirror MFP λ_μ (our previous assumption $\lambda_{\mathrm{fl}} = \lambda_\mu$ is not expected to hold in general), as well as the mean magnetised duration t_μ^*, which indicates the typical particle time scale of decoupling from field lines. The scaling $\lambda \sim \hat{\omega}_g^{-1/3}$ indicated in figure 7(*a*) serves purely as reference and should be taken with care, as small gyro radii with $\hat{\omega}_g \gtrsim 256$ are significantly affected by the MHD dissipation scales (compare also figure 1).

Our results clearly highlight the crucial role of coherent magnetic structures, especially for the low-energy regime, and support the role of field-line wandering in cosmic ray transport, as discussed by Pezzi & Blasi (2024). Further, highly magnetised low-energy particles such as GeV galactic cosmic rays are expected to be dynamically relevant on the plasma dynamics, requiring the consideration of streaming (Sampson *et al*. 2023).

To speculate about the asymptotic behaviour of the parameters of magnetised motion, we presume that the field line MFP $\lambda_{\parallel}$ for a particle with $\hat{\omega}_g$ is given by the average coherent curvature radius, i.e. the average of curvature radii larger than the typical gyro radius $(\pi/2)\hat{\omega}_g^{-1}$,

$$\lambda_{\parallel}(\hat{\omega}_g) = \left[\int_0^{\kappa_c} p(\hat{\kappa})\,\mathrm{d}\hat{\kappa}\right]^{-1} \int_0^{\kappa_c} \frac{p(\hat{\kappa})\,\mathrm{d}\hat{\kappa}}{\hat{\kappa}} \tag{4.1}$$

with $\kappa_c = (2/\pi)\hat{\omega}_g$. Following Lemoine (2023), we account for the influence of the magnetic field strength on the particle gyro radius by considering the compensated field-line curvature $\hat{\kappa} = \kappa/B$, whose distribution scales as $p(\hat{\kappa}) \sim \hat{\kappa}^{-2}$ (see also Baggaley *et al*. 2010; Yang *et al*. 2019; Bandyopadhyay *et al*. 2020). To compute (4.1), we assume the model distribution (motivated by Schekochihin *et al*. 2002)

$$p(\hat{\kappa}) = s(s-1)\kappa_0^{s-1}\frac{\hat{\kappa}}{(\kappa_0+\hat{\kappa})^{s+1}}, \tag{4.2}$$

which agrees well with our MHD simulation for $s = 2$ and $\kappa_0 = 1.5$, and yields $\lim_{\hat{\omega}_g\to\infty} \lambda_{\parallel}(\hat{\omega}_g) = \kappa_0^{-1}$.

Further, the path lengths between large-scale mirror events likely follow a broad distribution, which is truncated by the typical length of coherent field lines, so we remain with our assumption $\lambda_\mu \approx \lambda_{\parallel}$ for now. Given constant field-line and mirroring MFPs $\lambda_{\parallel} \approx \lambda_\mu \approx \kappa_0^{-1}$ in the low-energy limit, the asymptotic MFP is then solely determined by the decoupling time scale t_μ^*, which, in combination with compound subdiffusion of particles along coherent field lines, predicts $\lambda_{\mathrm{asymp}} \sim t_\mu^{*-1/2}$. As shown in figure 8(*a*), the durations of magnetised motion follow a broad power-law distribution with a long-time cut-off, which increases with decreasing particle energy. The asymptotic scaling of t_μ^* is not resolved in our data and can only be speculated about at the moment. For instance, $\lambda_{\mathrm{asymp}} \sim \hat{\omega}_g^{-1/3}$ would suggest $t_\mu^* \sim \hat{\omega}_g^{2/3}$. We expect it to arise from a complex interplay of lengths of coherent structures $\lambda_{\parallel}$, mirroring rates c/λ_μ, drift motions and possibly gyro-resonance due to Alfvén waves travelling along coherent flux tubes.

Further, as noted in § 2.2, the reported values for $\lambda_{\mathrm{asymp}} = D_\infty/v_{\mathrm{rms}}$ in figure 7(*a*) are biased by the periodic boundary conditions of the simulation domain (compare figure 6*a*). Despite this bias, our considerations clearly show that the value of D_∞ emerges from the short-time evolution of the particle distribution which is influenced by coherent structures on scales below the box size. Notably, these 'structure-mediated' values are larger than those obtained from random-phase turbulence (see also Shukurov *et al*. 2017; Lübke *et al*. 2024). However, on large scales $\gg L_{\mathrm{box}}$, such as the ISM or ICM outer scales, this structure-mediated enhancement has to be weighted against confinement in structures if scattering is rare and t_μ^* is large.

4.2. *Discussion of coherent structures*

Despite the idealised nature of our turbulence set-up, consisting of a visco-resistive incompressible MHD simulation with $Re_T \sim O(100)$ and $Pr = \nu/\eta = 1$, our results can be contextualised with coherent structures ubiquitously found in simulations and observations (see, e.g. Robitaille *et al*. 2020; Ntormousi *et al*. 2024). The fluctuating dynamo with compressible (Beattie *et al*. 2024) or kinetic (St-Onge & Kunz

2018) physics also exhibits pronounced coherent structures, although their statistics, such as $p(B, \kappa)$, likely differ from our case and a dedicated study of cosmic-ray transport in these cases would be useful. While our focus has been on intense flux tubes generated by the fluctuating dynamo, coherent structures also emerge as patch-wise aligned states due to selective decay (Matthaeus *et al*. 2015; Hosking & Schekochihin 2021; see also figure 3) or as intense aligned wave packets in critically balanced turbulence (Perez & Boldyrev 2009; Chandran, Schekochihin & Mallet 2015). Generally, different turbulence set-ups (e.g. forced or freely decaying, with or without an imposed background magnetic field, different degrees of compressibility, cross- and magnetic helicity) lead to different predominant kinds of structures, which may impact cosmic-ray transport in different ways. Here, we use the term 'structure' to loosely summarise relatively coherent phenomena with nonlinear qualities (see also Grošelj *et al*. (2019) for a different, but not contradictory, point of view).

Current sheets emerge as the unifying feature of these various kinds of turbulence (see, e.g. Servidio *et al*. 2011; Zhdankin, Boldyrev & Uzdensky 2016), which, given sufficient dynamical range, become tearing-unstable, leading to fast reconnection and the seeding of small-scale plasmoid chains, i.e. complexes of highly tangled small-scale flux tubes. This process is associated with a reconnection-mediated turbulence regime at the transition to kinetic scales (Loureiro & Boldyrev 2017; Mallet, Schekochihin & Chandran 2017; Chernoglazov, Ripperda & Philippov 2021; Dong *et al*. 2022), which has important implications on cosmic-ray acceleration (Comisso & Sironi 2019) and may be relevant for a transport theory of the lowest-energy cosmic rays or suprathermal particle populations. However, particular care must be taken when analysing simulations featuring plasmoids, such as ours, because they may also appear as numerical artefacts for insufficient numerical resolution (Morillo & Alexakis 2025).

Understanding these various structures and their interaction with charged particles is crucial for a comprehensive picture of cosmic-ray transport in realistic multiphase media (Armillotta, Ostriker & Jiang 2022; Beattie *et al*. 2025). Also, given sufficiently high numerical resolution, gyro-resonance can be expected to re-appear, for instance, mediated by small-scale Alfvén wave turbulence emerging along coherent flux tubes, either as part of the turbulent cascade or self-generated by cosmic rays. A new cosmic-ray transport theory should carefully weigh these different processes and their varying predominance against each other (Hopkins *et al*. 2022; Kempski & Quataert 2022).

4.3. *Synthetic turbulence*

Synthetic turbulence refers to a class of algorithms designed for overcoming the limited resolvable range of scales of first-principles simulations. They provide fast generation of random fields resembling certain statistics expected for realistic turbulence. Most commonly, guided by the paradigm of gyro-resonance, these fields are synthesised from a prescribed energy spectrum and random Fourier phases (see, e.g. Mertsch 2020). These random-phase models have well-known shortcomings, such as the inability to reproduce intermittency and coherent structures, as illustrated by, e.g. Shukurov *et al*. (2017), which has led to the exploration of intermittent and structured models (Subedi *et al*. 2014; Pucci *et al*. 2016; Durrive *et al*. 2022; Lübke *et al*. 2024; Maci, Keppens & Bacchini 2024; Lesaffre *et al*. 2025). To address the crucial geometric structure, future synthetic models for strong isotropic turbulence should include the field-line curvature distribution $p(\kappa) \sim \kappa^{-5/2}$ as well as the anti-correlation between magnetic field strength and field-line curvature

$B \sim \kappa^{-1/2}$. Instead of generating a synthetic field directly, generative diffusion models, a recently developed machine learning technique, are able to learn and synthesise particle trajectories directly (Li *et al*. 2023; Martin *et al*. 2025). Such a technique could also be useful for classifying the various transport behaviours and refining the heuristic magnetisation criterion $\bar{\kappa}\bar{r}_g \sim 1$.

5. Outlook

5.1. *Refinement of the combined stochastic model*

We emphasise that our model is semi-empirical, where parameters are inferred from the test-particle data. It is essential for a proper transport theory to predict the involved MFPs and mean durations from the underlying turbulence. In particular, such a theory should account for the hierarchy of scales present in the problem, from scattering on gyro scales, over motion within individual coherent structures and up to large-scale network-like constellations of the population of coherent structures (Ntormousi *et al*. 2024). This task could be approached by projector-based coarse-graining of the dynamics, following the Mori–Zwanzig formalism (Hudson & Li 2020; Lin *et al*. 2021).

Another possible approach to accurately derive the required MFPs and mean durations would be to follow Drummond (1982) and start with a path integral formulation of turbulent diffusion. However, in Drummond's approach, the magnetic potential is assumed to be Gaussian. A possible, far from trivial approach would be a path integral formulation including the action S_{MHD} corresponding to the MHD dynamics plus the action S_{particle} of the particle dynamics and applying non-perturbative methods to approximate this complex path integral (see, e.g. Grafke, Grauer & Schäfer 2015; Bureković *et al*. 2024; Schorlepp & Grafke 2025).

5.2. *Alternative transport descriptions*

A central assumption of our model is that all involved kinds of motion are Gaussian and sufficiently characterised by their MFPs or MSDs. While our combined model of Langevin and compound subdiffusion successfully reproduces the test-particle MSD, possibly relevant higher-order statistics are neglected. For instance, intermittent pitch-angle scattering (Zimbardo & Perri 2020) or streaming (Sampson *et al*. 2023) can lead to superdiffusion of cosmic rays. In the context of our test-particle data, magnetised motion may be described by spatial superdiffusion (averaged over the pitch angle), and mirror-confinement in coherent structures may correspond to subdiffusion. A clever combination of Lévy walks and extended waiting times (Zaburdaev, Denisov & Klafter 2015) with truncated distributions (Liang & Oh 2025) may reproduce the intricate time evolution of the test-particle MSDs, while also accounting for possibly relevant higher-order statistics. In this case of competition between sub- and superdiffusion (Magdziarz & Weron 2007) of cosmic rays, a single (fractional) transport equation might be formulated that is equivalent to the stochastic model as presented for the superdiffusive case by Effenberger *et al*. (2024) and Aerdker *et al*. (2025).

Alternatively, especially when modelling large-scale ($\gg L_u$) multiphase media, the structured nature of turbulence may be reflected by distinct diffusion coefficients. For the example of two spatially distinguishable phases, one can employ a regular Fokker–Planck equation $\partial_t f(\boldsymbol{x}, t) = \Delta D(\boldsymbol{x}) f(\boldsymbol{x}, t)$ with a mixed diffusion coefficient $D(\boldsymbol{x}) = D_1$ for $\boldsymbol{x} \in$ phase 1 and $D(\boldsymbol{x}) = D_2$ for $\boldsymbol{x} \in$ phase 2, which is readily applicable to astrophysical problems (see, e.g. Reichherzer *et al*. 2025). Otherwise,

a temporal switching Fokker–Planck equation $\partial_t f_i(\boldsymbol{x}, t) = D_i \Delta f_i(\boldsymbol{x}, t) + A_{ij} f_j(\boldsymbol{x}, t)$ with Markovian switching rates A_{ij} may be useful (see, e.g. Bressloff & Lawley 2017; Balcerek *et al*. 2023), which could be applied as a sub-grid model for cosmic-ray transport.

All presented models involve a competition between two transport regimes to capture the transient phases of the observed MSD. Similar switching or competing models are also known in other complex systems (see, e.g. Doerries, Chechkin & Metzler 2022; Datta, Beta & Großmann 2024).

5.3. *Generalised transport equation*

To study structure-mediated transport of cosmic rays in astrophysical applications, the physics described by our combined stochastic model needs to be encapsulated in a generalised transport equation for the 5 + 1-dimensional particle distribution function $f(\boldsymbol{x}, \mu, \hat{\omega}_g, t)$. This transport equation takes the form $\partial_t f = \mathcal{D}[f]$, where the generalised transport operator $\mathcal{D}[\cdot]$ can describe a wide range and combination of processes, such as (anomalous) spatial diffusion $\mathcal{D} = D_{xx} \Delta^{(\alpha)}$, pitch-angle diffusion $\mathcal{D} = \partial_\mu D_{\mu\mu} \partial_\mu$ or momentum diffusion $\mathcal{D} = p^{-2} \partial_p p^2 D_{pp} \partial_p$ (with momentum $p \propto \hat{\omega}_g$ in our notation) (Metzler & Klafter 2000; Schlickeiser 2002). Since transport properties are strong functions of the local plasma conditions and cosmic rays can exert a dynamically relevant feedback on the plasma, the transport equation needs to be coupled with the astrophysical simulation for a self-consistent treatment (Bai *et al*. 2015; Pfrommer *et al*. 2017; Böss *et al*. 2023). With such a set-up, one could, for instance, study the effect of streaming on coherent structures (compare, e.g. Rieder & Teyssier 2017; Sampson *et al*. 2023).

Possible approaches to construct an operator $\mathcal{D}$, which describes the competition between two modes of transport, are contemplated in § 5.2. We also note that $\mathcal{D}$ must not necessarily be known explicitly, as it can be represented and solved by the corresponding stochastic differential equations (Effenberger *et al*. 2024; Aerdker *et al*. 2025). The remaining challenge is then to parametrise our transport model in terms of characteristic turbulence quantities, which may vary across the large-scale simulation domain, such as the turbulence correlation scale, turbulence strength or sonic Mach number.

Such an integrated study can provide data for validating this or other non-standard transport models against observational data. Ultimately, this study should not only be consistent with the data, but provide falsifiable predictions. Observational constraints for intermittent cosmic-ray scattering theories are, for instance, considered by Butsky *et al*. (2024) and Kempski *et al*. (2025).

6. Summary

To gain a deeper understanding of the transport of highly energetic charged particles, such as cosmic rays, through isotropic structured magnetic turbulence, we studied the motion of test particles in snapshots obtained from a magnetohydrodynamic simulation of a saturated fluctuating dynamo. Based on a careful analysis of the data, we propose a model that separates particle motion into two distinct modes: non-diffusive magnetised transport along strong coherent flux tubes, and diffusive unmagnetised transport in weak and highly tangled regions of the magnetic field. We present a stochastic process for each mode, parametrised by separate mean free paths for coherent field line wandering, large-scale mirroring and unmagnetised scattering. The global transport behaviour emerging from the competition of these

processes is described by a combined model, which consists of a stochastic walker that alternates between the two transport modes, where the duration of each segment is sampled from the respective escape-time probability distribution.

The central result of our study is that this combined model accurately reproduces the time-dependent test-particle mean squared displacements, thus providing an explanation for the observed behaviour. Specifically, field-line wandering and large-scale mirroring with long mean free paths along coherent structures give rise to compound subdiffusion, accounting for the pronounced initial ballistic phase and the transient subdiffusive phase. Intermittent scattering and unmagnetised motion with short mean free paths facilitate cross-field transport, giving rise to asymptotically diffusive behaviour.

The regime of particle energies, which is currently numerically accessible, is clearly non-asymptotic, i.e. the energy-dependent scaling of the unconditional mean free path does not yet exhibit the expected low-energy power-law behaviour. However, our results reveal a clear tendency towards the dominance of magnetised motion at small energies, which implies that field-line wandering, non-resonant mirroring and decoupling of particles from field lines due to intermittent encounters with sharp curvatures are the primary mechanisms for cosmic-ray transport in the asymptotic low-energy regime. We emphasise that their modelling should be done with care to appropriately account for the highly complex nature of structured turbulence, which is evident in the vastly different length scales characterising individual structures (long coherence lengths and sharp folds), as well as non-trivial correlations between separate structures.

Acknowledgements

We gratefully acknowledge helpful discussions with Martin Lemoine, as well as the warm hospitality of Gaetano Zimbardo and Silvia Perri, who organised stimulating workshops at the University of Calabria in September 2024 and February 2025. J.L. is grateful to Alex Schekochihin and Luca Biferale for the opportunities to present and discuss early stages of this work at the University of Oxford in July 2023 and at the University of Rome Tor Vergata in March 2024, respectively. J.L., P.R. and S.A. would like to acknowledge the Princeton Center for Theoretical Science for hosting the stimulating workshop ‘Synergistic approaches to particle transport in magnetised turbulence: from the laboratory to astrophysics’ in April 2024. The authors also thank the anonymous referee, whose comments helped to improve this manuscript.

Editor Antoine C. Bret thanks the referees for their advice in evaluating this article.

Funding

This work was supported by the Deutsche Forschungsgemeinschaft (DFG, German Research Foundation) through the Collaborative Research Center SFB1491 ‘Cosmic Interacting Matters – From Source to Signal’ (grant no. 445052434); and the International Space Science Institute (ISSI) in Bern through ISSI International Team project #24-608 ‘Energetic Particle Transport in Space Plasma Turbulence’. The work of P.R. was initially funded through a Gateway Fellowship and subsequently by the DFG through the Walter Benjamin Fellowship (grant no. 518672034). F.E. acknowledges partial support from NASA LWS grant 80NSSC21K1327. The authors gratefully acknowledge the Gauss Centre for Supercomputing e.V. (www.gauss-centre.eu) for funding this project by providing computing time on the

SuperMUC-NG at Leibniz Supercomputing Centre (www.lrz.de) and through the John von Neumann Institute for Computing (NIC) on the GCS Supercomputers JUWELS at Jülich Supercomputing Centre (JSC).

Declaration of interests

The authors report no conflict of interest.

Appendix A. Non-dimensionalisation of the relativistic Newton–Lorentz equations

The relativistic Newton–Lorentz equations are given by

$$\dot{\boldsymbol{X}}_t = \boldsymbol{V}_t, \quad \dot{\boldsymbol{P}}_t = \frac{q}{m}\left(\boldsymbol{E}(\boldsymbol{X}_t) + \boldsymbol{V}_t \times \boldsymbol{B}(\boldsymbol{X}_t)\right) \tag{A1}$$

with the relativistic particle momentum $\boldsymbol{P}_t = \gamma(V_t)\boldsymbol{V}_t$. By writing amplitudes and normalised quantities separately, and re-arranging

$$\frac{V_0}{T_0}\frac{\mathrm{d}\hat{\boldsymbol{P}}_t}{\mathrm{d}\hat{t}} = \frac{q}{m}V_0 B_{\mathrm{rms}}\hat{\boldsymbol{V}}_t \times \hat{\boldsymbol{B}}(\boldsymbol{X}_t) + \frac{q}{m}E_{\mathrm{rms}}\hat{\boldsymbol{E}}(\boldsymbol{X}_t),$$

$$\frac{\mathrm{d}\hat{\boldsymbol{P}}_t}{\mathrm{d}\hat{t}} = \alpha\hat{\boldsymbol{V}}_t \times \hat{\boldsymbol{B}}(\boldsymbol{X}_t) + \beta\hat{\boldsymbol{E}}(\boldsymbol{X}_t), \tag{A2}$$

we can introduce the coupling constants

$$\alpha = \frac{q}{m}\frac{L_0 B_{\mathrm{rms}}}{V_0}, \quad \beta = \frac{q}{m}\frac{L_0 E_{\mathrm{rms}}}{V_0^2}, \tag{A3}$$

where we replaced the characteristic time T_0 by the outer scale $L_0 = V_0 T_0$. In the limit $E_{\mathrm{rms}} \ll V_0$, the particle energy is conserved, $\gamma(V_t) = \text{const.}$, and we can write

$$\dot{\boldsymbol{V}}_t = \frac{\mathrm{d}\boldsymbol{V}_t}{\mathrm{d}t} = \hat{\omega}_g \boldsymbol{V}_t \times \boldsymbol{B}(\boldsymbol{X}_t), \tag{A4}$$

where the hats $\hat{\cdot}$ are dropped for notational convenience, and we obtain the normalised gyro frequency

$$\hat{\omega}_g = \frac{\alpha}{\gamma} = \frac{q B_{\mathrm{rms}} L_0}{\gamma m v_0}. \tag{A5}$$

Appendix B. Alternative magnetisation criterion

In addition to the magnetic moment variation conditional on the regular curvature, as given by (2.8), we also study the dependence on the perpendicular reversal scale (Kempski *et al.* 2023)

$$\kappa_\perp = \frac{\|(\nabla \times \boldsymbol{B}) \times \boldsymbol{B} - \boldsymbol{B}/B \times (\boldsymbol{B} \cdot \nabla \boldsymbol{B})\|}{B^2} = \frac{\|\boldsymbol{B} \times (\boldsymbol{B} \times \nabla \log B)\|}{B^2}. \tag{B1}$$

The results are shown in figure 11, and the decision boundary at $\overline{\delta M}/\overline{M} \sim 1$ is roughly described by

$$\bar{\kappa}_\perp \bar{r}_g^{1/2} \sim 30. \tag{B2}$$

Although this decision boundary appears to be cleaner when compared with figure 5, transport statistics conditional on $\kappa_\perp$ do not yield significant improvements when compared with κ, especially in respect to the bias of the magnetised data. Additionally, the criterion given by (B2) does not convey the compelling physical interpretation of $\bar{\kappa}\bar{r}_g \sim 1$.

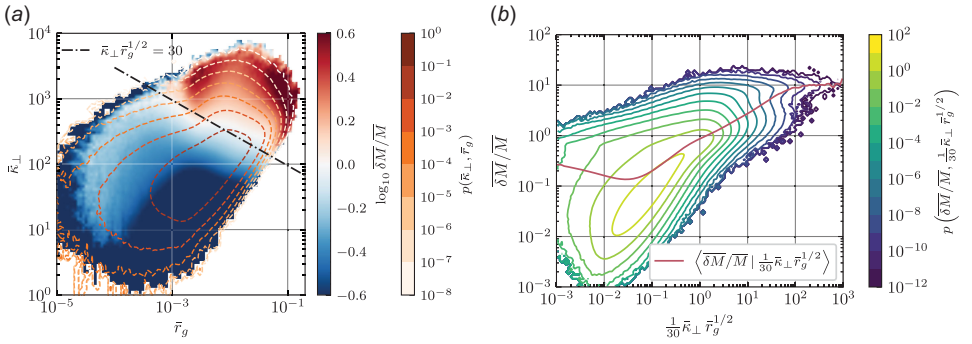

FIGURE 11. (*a*) Average of the relative magnetic moment variation $\delta\overline{M}/\overline{M}$ conditional on the particle gyro radius $\bar{r}_g$ and the field-line perpendicular reversal scale $\kappa_\perp$. The transition region $\delta\overline{M}/\overline{M} \sim 1$ between magnetised and unmagnetised transport is approximately described by $\bar{\kappa}_\perp \bar{r}_g^{1/2} \sim 30$. The joint density $p(\bar{\kappa}_\perp, \bar{r}_g)$ is indicated for reference. The remarks for the colour scale of figure 5 apply here as well. (*b*) Joint density of the relative magnetic moment variation $\delta\overline{M}/\overline{M}$ and perpendicular magnetisation criterion $(1/30)\bar{\kappa}_\perp \bar{r}_g^{1/2}$, as well as the conditional average $\langle \delta\overline{M}/\overline{M} | (1/30)\bar{\kappa}_\perp \bar{r}_g^{1/2} \rangle$.

Appendix C. Derivations of MSD expressions

C.1 *Langevin equation*

We consider the Langevin equation

$$\mathrm{d}\boldsymbol{X}_s = \boldsymbol{V}_s \,\mathrm{d}s, \quad \mathrm{d}\boldsymbol{V}_s = -\theta \boldsymbol{V}_s \,\mathrm{d}s + \sqrt{\frac{2\theta v_{\mathrm{rms}}^2}{3}}\,\mathrm{d}\boldsymbol{W}_s, \tag{C1}$$

with initial conditions $X_{i,0} = 0$ and $V_{i,0} \sim \mathcal{N}(0, v_{\mathrm{rms}}^2/3)$, and uncorrelated Gaussian noise $\langle \mathrm{d}W_{i,s}\,\mathrm{d}W_{j,s'}\rangle = \delta_{ij}\delta(s-s')$. The formal solutions of the components of $\boldsymbol{X}_s$ and $\boldsymbol{V}_s$ can be written as

$$X_{i,s} = \int_0^s V_{i,s'}\,\mathrm{d}s', \quad V_{i,s} = \sqrt{\frac{2\theta v_{\mathrm{rms}}^2}{3}} \int_{-\infty}^s e^{-\theta(s-s')}\,\mathrm{d}W_{s'}, \tag{C2}$$

where the initial conditions are reflected in the lower integral limits. The auto-covariance function of $V_{i,s}$ can be computed by means of the Itô isometry as

$$\begin{aligned}
\langle V_{i,r} V_{i,s}\rangle &= \frac{2\theta v_{\mathrm{rms}}^2}{3} e^{-\theta(r+s)} \left\langle \int_{-\infty}^r \int_{-\infty}^s e^{\theta r'} e^{\theta s'}\,\mathrm{d}W_{r'}\,\mathrm{d}W_{s'} \right\rangle \\
&= \frac{2\theta v_{\mathrm{rms}}^2}{3} e^{-\theta(r+s)} \int_{-\infty}^{\min(r,s)} \int_{-\infty}^{\min(r,s)} e^{\theta r'} e^{\theta s'}\,\mathrm{d}r'\,\mathrm{d}s' \\
&= \frac{2\theta v_{\mathrm{rms}}^2}{6\theta} e^{-\theta(r+s)} e^{2\theta \min(r,s)} \\
&= \frac{v_{\mathrm{rms}}^2}{3} e^{-\theta|r-s|},
\end{aligned} \tag{C3}$$

which can then be used to find the variance of $X_{i,s}$ as

$$\begin{aligned}
\langle X_{i,s}^2 \rangle &= \int_0^s \int_0^s \langle V_{i,s'} V_{i,s''} \rangle \, \mathrm{d}s' \, \mathrm{d}s'' \\
&= \frac{v_{\mathrm{rms}}^2}{3} \int_0^s \int_0^s e^{-\theta |s'-s''|} \, \mathrm{d}s' \, \mathrm{d}s'' \\
&= \frac{v_{\mathrm{rms}}^2}{3} \int_0^s \left(\int_0^{s'} e^{-\theta(s'-s'')} \, \mathrm{d}s'' + \int_{s'}^s e^{-\theta(s''-s')} \, \mathrm{d}s'' \right) \mathrm{d}s' \\
&= \frac{v_{\mathrm{rms}}^2}{3} \int_0^s \left(e^{-\theta s'} \frac{e^{\theta s'} - 1}{\theta} - e^{\theta s'} \frac{e^{-\theta s} - e^{-\theta s'}}{\theta} \right) \mathrm{d}s' \\
&= \frac{v_{\mathrm{rms}}^2}{3\theta} \int_0^s \left(2 - e^{-\theta s'} - e^{-\theta(s-s')} \right) \mathrm{d}s' \\
&= \frac{v_{\mathrm{rms}}^2}{3\theta} \left(2s + \frac{e^{-\theta s} - 1}{\theta} - e^{-\theta s} \frac{e^{\theta s} - 1}{\theta} \right) \\
&= \frac{2 v_{\mathrm{rms}}^2}{3\theta^2} \left(e^{-\theta s} + \theta s - 1 \right). \qquad \text{(C4)}
\end{aligned}$$

The variance is equivalent to the MSD, because the processes have zero mean and the initial position is fixed to $X_{i,0} = 0$.

C.2 *Compound subdiffusion*

We find the MSD of the subordinated process

$$\boldsymbol{Y}_t = \boldsymbol{X}_{\mathrm{fl},s_t} \qquad \text{(C5)}$$

by computing the average MSD of $\boldsymbol{X}_{\mathrm{fl},s}$ weighted by the displacement s_t at time t

$$\left\langle Y_t^2 \right\rangle = \int_{-\infty}^{+\infty} \left\langle X_{\mathrm{fl},|s|}^2 \right\rangle \frac{1}{\sqrt{2\pi \langle s_t^2 \rangle}} \exp\left(-\frac{s^2}{2\langle s_t^2 \rangle} \right) \mathrm{d}s, \qquad \text{(C6)}$$

where we assume a Gaussian distribution for s_t. For the short-time asymptotic behaviour, we recall $\langle X_s^2 \rangle \underset{s \to 0}{\sim} v_{\mathrm{rms}}^2 s^2$ and $\langle s_t^2 \rangle \underset{t \to 0}{\sim} v_{\mathrm{eff}}^2 t^2/3$, for which we can evaluate the integral as

$$\begin{aligned}
\langle Y_t^2 \rangle &\underset{t \to 0}{\sim} \int_{-\infty}^{+\infty} v_{\mathrm{rms}}^2 s^2 \frac{1}{\sqrt{2\pi \, v_{\mathrm{eff}}^2 t^2/3}} \exp\left(-\frac{s^2}{2 v_{\mathrm{eff}}^2 t^2/3} \right) \mathrm{d}s \\
&= \frac{v_{\mathrm{rms}}^2}{\sqrt{2\pi}} \frac{\sqrt{3}}{v_{\mathrm{eff}} t} \int_{-\infty}^{+\infty} s^2 \exp\left(-\frac{3s^2}{2 v_{\mathrm{eff}}^2 t^2} \right) \mathrm{d}s
\end{aligned}$$

$$= \frac{v_{\mathrm{rms}}^2}{\sqrt{2\pi}} \frac{\sqrt{3}}{v_{\mathrm{eff}} t} \frac{\sqrt{\pi}}{2\left(3/2 v_{\mathrm{eff}}^2 t^2\right)^{3/2}}$$

$$= \frac{v_{\mathrm{rms}}^2 v_{\mathrm{eff}}^2 t^2}{3}. \tag{C7}$$

Additionally, for the long-time asymptotic behaviour with $\langle X_s^2 \rangle \underset{s\to\infty}{\sim} 2v_{\mathrm{rms}}^2 s/\theta$ and $\langle s_t^2 \rangle \underset{t\to\infty}{\sim} 2v_{\mathrm{eff}}^2 t/3\theta_\mu$, we can work out

$$\langle Y_t^2 \rangle \underset{t\to\infty}{\sim} \int_{-\infty}^{+\infty} \frac{2v_{\mathrm{rms}}^2 |s|}{\theta} \frac{1}{\sqrt{4\pi\, v_{\mathrm{eff}}^2 t/3\theta_\mu}} \exp\left(-\frac{s^2}{4v_{\mathrm{eff}}^2 t/3\theta_\mu}\right) \mathrm{d}s$$

$$= \frac{v_{\mathrm{rms}}^2 \sqrt{3\theta_\mu}}{v_{\mathrm{eff}} \theta \sqrt{\pi t}} \int_{-\infty}^{+\infty} |s| \exp\left(-\frac{3\theta_\mu s^2}{4v_{\mathrm{eff}}^2 t}\right) \mathrm{d}s$$

$$= \frac{v_{\mathrm{rms}}^2 \sqrt{3\theta_\mu}}{v_{\mathrm{eff}} \theta \sqrt{\pi t}} \sqrt{\pi} \frac{4v_{\mathrm{eff}}^2 t}{3\theta_\mu}$$

$$= \frac{4v_{\mathrm{rms}}^2 v_{\mathrm{eff}} \sqrt{t}}{\theta \sqrt{3\theta_\mu}}$$

$$= \frac{4v_{\mathrm{rms}} \lambda_{\mathrm{fl}} \sqrt{v_{\mathrm{eff}} \lambda_\mu t}}{3}, \tag{C8}$$

where we made use of the MFP expressions $\lambda_{\mathrm{fl}} = v_{\mathrm{rms}}/\theta$ and $\lambda_\mu = v_{\mathrm{eff}}/\theta_\mu$.

Appendix D. Bayesian optimisation

Optimising the loss function given by (3.14) requires the simulation of a sufficiently large number of samples of our combined stochastic model given by Algorithm 1 at each step of the optimisation procedure. The number of samples needs to be large enough to produce a sufficiently converged average $\langle \Delta Z_{\mathrm{model},\tau}^2 \rangle$, but also small enough to remain within reasonable computational cost. However, even for a carefully chosen number of samples, evaluating (3.14) remains relatively expensive and noisy.

We therefore turn to Bayesian optimisation as implemented in the software package `scikit-optimize` (Head *et al.* 2021), which treats evaluations of the loss function as samples drawn from a Gaussian process. Based on previous observations, a cheap acquisition function is optimised, which gives the next point in the parameter space to evaluate. In this way, a reliable estimate of the optimal parameters is achievable for a small number of evaluations of the loss function. The procedure additionally provides a hyper-parameter ξ to balance exploration of uncertain regions of the parameter space against exploitation of regions, which likely contain a minimum of the loss function.

For each $\hat{\omega}_g$, we run 64 steps with $\xi = 1$ for exploration, followed by 64 steps with $\xi = 0.01$ for exploitation of likely minima. For 96 000 samples of the combined stochastic model, distributed on 96 CPU cores, a single evaluation of the loss function takes approximately 35 seconds. The resulting loss functions are shown in figure 12, including the expected minima and roughly estimated confidence intervals.

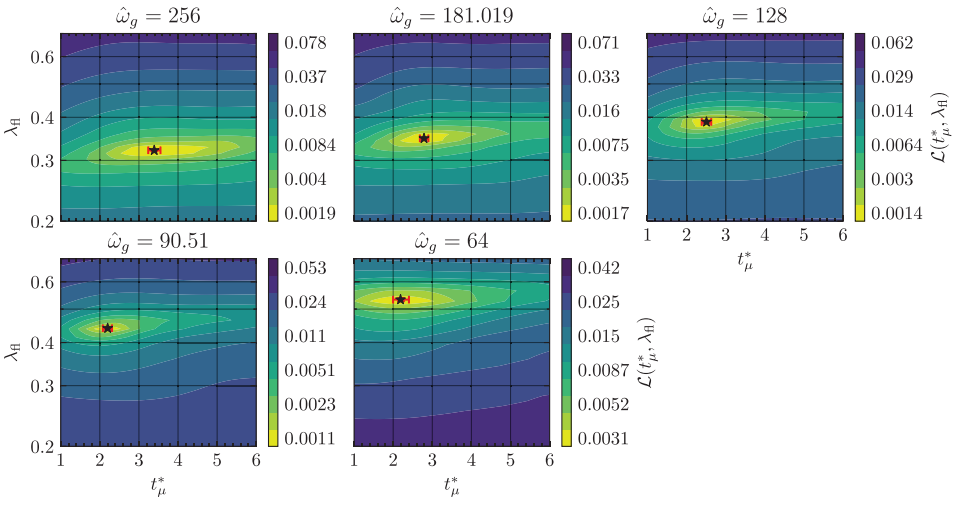

FIGURE 12. Landscapes of the loss function (3.14) as estimated by Bayesian optimisation, including the expected minimum and estimated confidence intervals.

Confidence intervals for Bayesian optimisation are not provided by the software package and hard to find in the literature. We thus produce, for each $\hat{\omega}_g$, a naive estimate based on 480 independent realisations of the underlying trained Gaussian process. The realisations are generated for random points on the parameter grid in the neighbourhood of the expected minimum and the minimum of each realisation is recorded. The mean of the minima of the realisations converges to the expected minimum and their standard deviation is taken as confidence bounds on the parameters.

REFERENCES

AERDKER, S., MERTEN, L., EFFENBERGER, F., FICHTNER, H., BECKER TJUS, J. & 2025 Superdiffusion of energetic particles at shocks: a Lévy flight model for acceleration. *A& A* **693**, A15.

ALBRIGHT, B. J., CHANDRAN, B. D. G., COWLEY, S. C. & LOH, M. 2001 Parallel heat diffusion and subdiffusion in random magnetic fields. *Phys. Plasmas* **8**, 777–787.

ALVELIUS, K. 1999 Random forcing of three-dimensional homogeneous turbulence. *Phys. Fluids* **11**, 1880–1889.

AMATO, E. & BLASI, P. 2018 Cosmic ray transport in the galaxy: a review. *Adv. Space Res.* **62**, 2731–2749.

ARMILLOTTA, L., OSTRIKER, E.C. & JIANG, Y.-F. 2022 Cosmic-ray transport in varying galactic environments. *ApJ* **929**, 170.

ARZNER, K., KNAEPEN, B., CARATI, D., DENEWET, N. & VLAHOS, L. 2006 The effect of coherent structures on stochastic acceleration in MHD turbulence. *ApJ* **637**, 322–332.

BAGGALEY, A. W., SHUKUROV, A., BARENGHI, C. F. & SUBRAMANIAN, K. 2010 Fluctuation dynamo based on magnetic reconnections. *Astron. Nachr.* **331**, 46.

BAI, X.-N., CAPRIOLI, D., SIRONI, L. & SPITKOVSKY, A. 2015 Magnetohydrodynamic-particle-in-cell method for coupling cosmic rays with a thermal plasma: application to non-relativistic shocks. *ApJ* **809**, 55.

BALCEREK, M., WYŁOMAŃSKA, A., BURNECKI, K., METZLER, R. & KRAPF, D. 2023 Modelling intermittent anomalous diffusion with switching fractional Brownian motion. *New J. Phys.* **25**, 103031.

BALESCU, R., WANG, H.-D. & MISGUICH, J. H. 1994 Langevin equation versus kinetic equation: subdiffusive behavior of charged particles in a stochastic magnetic field. *Phys. Plasmas* **1**, 3826–3842.

BANDYOPADHYAY, R., *et al.* 2020 In situ measurement of curvature of magnetic field in turbulent space plasmas: a statistical study. *ApJ* **893**, L25.

BEATTIE, J.R., FEDERRATH, C., KLESSEN, R.S., CIELO, S. & BHATTACHARJEE, A. 2024 Magnetized compressible turbulence with a fluctuation dynamo and Reynolds numbers over a million. arXiv:2405.16626

BEATTIE, J.R., KOLBORG, N., ANNE, R.-R., Enrico, & FEDERRATH, C. 2025 So long Kolmogorov: the forward and backward turbulence cascades in a supernovae-driven, multiphase interstellar medium. arXiv:2501.09855

BELL, A. R., MATTHEWS, J. H., TAYLOR, A. M. & GIACINTI, G. 2025 Cosmic ray transport and acceleration with magnetic mirroring. *MNRAS* **539**, 1236–1247.

BERESNYAK, A., YAN, H. & LAZARIAN, A. 2011 Numerical study of cosmic ray diffusion in magneto-hydrodynamic turbulence. *ApJ* **728**, 60.

BIAN, N. H. & LI, G. 2024 Lagrangian perspectives on the small-scale structure of Alfvénic turbulence and stochastic models for the dispersion of fluid particles and magnetic field lines in the solar wind. *ApJS* **273**, 15.

BISKAMP, D. 2003 *Magnetohydrodynamic Turbulence*. Cambridge University Press.

BOLDYREV, S. 2006 Spectrum of magnetohydrodynamic turbulence. *Phys. Rev. Lett.* **96**, 115002.

BORIS, J.P. & SHANNY, R.A. 1971 Proceedings, Fourth Conference on Numerical Simulation of Plasmas. Naval Research Laboratory.

BÖSS, L.M., STEINWANDEL, U.P., DOLAG, K. & LESCH, H. 2023 CRESCENDO: an on-the-fly Fokker–Planck solver for spectral cosmic rays in cosmological simulations. *MNRAS* **519**, 548–572.

BRANCH, M.A., COLEMAN, T.F. & LI, Y. 1999 A subspace, interior, and conjugate gradient method for large-scale bound-constrained minimization problems. *SIAM J. Sci. Comput.* **21**, 1–23.

BRANDENBURG, A. & SARSON, G.R. 2002 Effect of hyperdiffusivity on turbulent dynamos with helicity. *Phys. Rev. Lett.* **88**, 055003.

BRESSLOFF, P.C. & LAWLEY, S.D. 2017 Temporal disorder as a mechanism for spatially heterogeneous diffusion. *Phys. Rev. E* **95**, 060101.

BUREKOVIĆ, S., SCHÄFER, T. & GRAUER, R. 2024 Instantons, fluctuations, and singularities in the supercritical stochastic nonlinear schrödinger equation. *Phys. Rev. Lett.* **133**, 077202.

BUTSKY, I.S., HOPKINS, P.F., KEMPSKI, P., PONNADA, S.B., QUATAERT, E. & SQUIRE, J. 2024 Galactic cosmic-ray scattering due to intermittent structures. *MNRAS* **528**, 4245–4254.

CHANDRAN, B.D.G., COWLEY, S.C., IVANUSHKINA, M. & SYDORA, R. 1999 Heat transport along an inhomogeneous magnetic field. I. Periodic magnetic mirrors. *ApJ* **525**, 638–650.

CHANDRAN, B. D. G., SCHEKOCHIHIN, A. A. & MALLET, A. 2015 Intermittency and alignment in strong RMHD turbulence. *ApJ* **807**, 39.

CHANDRASEKHAR, S. 1943 Stochastic problems in physics and astronomy. *Rev. Mod. Phys.* **15**, 1–89.

CHECHKIN, A.V., SENO, F., METZLER, R. & SOKOLOV, I.M. 2017 Brownian yet non-gaussian diffusion: from superstatistics to subordination of diffusing diffusivities. *Phys. Rev. X* **7**, 021002.

CHEN, C. H. K., *et al.* 2020 The evolution and role of solar wind turbulence in the inner heliosphere. *ApJS* **246**, 53.

CHERNOGLAZOV, A., RIPPERDA, B. & PHILIPPOV, A. 2021 Dynamic alignment and plasmoid formation in relativistic magnetohydrodynamic turbulence. *ApJ* **923**, L13.

COHET, R. & MARCOWITH, A. 2016 Cosmic ray propagation in sub-Alfvénic magnetohydrodynamic turbulence. *A&A* **588**, A73.

COMISSO, L. & SIRONI, L. 2019 The interplay of magnetically dominated turbulence and magnetic reconnection in producing nonthermal particles. *ApJ* **886**, 122.

CRUTCHER, R.M. 2012 Magnetic fields in molecular clouds. *ARA& A* **50**, 29–63.

DATTA, A., BETA, C. & GROSSMANN, R. 2024 Random walks of intermittently self-propelled particles. *Phys. Rev. Res.* **6**, 043281.

DOERRIES, T., CHECHKIN, A. V. & METZLER, R. 2022 Apparent anomalous diffusion and non-Gaussian distributions in a simple mobile-immobile transport model with Poissonian switching. arXiv:2203.13328

DONG, C., WANG, L., HUANG, Y.-M., COMISSO, L., SANDSTROM, T.A. & A., BHATTACHARJEE 2022 Reconnection-driven energy cascade in magnetohydrodynamic turbulence. *Sci. Adv.* **8**, eabn7627.

DÖRNER, J., REICHHERZER, P., TJUS, B., Julia, & HEESEN, V. 2023 Cosmic-ray electron transport in the galaxy M 51. *A&A* **669**, A111.

DRUMMOND, I. T. 1982 Path-integral methods for turbulent diffusion. *J. Fluid Mech.* **123**, 59–68.

DURRIVE, J.-B., CHANGMAI, M., KEPPENS, R., LESAFFRE, P., MACI, D. & MOMFERATOS, G. 2022 Swift generator for three-dimensional magnetohydrodynamic turbulence. *Phys. Rev. E* **106**, 025307.

EFFENBERGER, F., AERDKER, S., MERTEN, L. & H., FICHTNER 2024 Superdiffusion of energetic particles at shocks: a fractional diffusion and Lévy flight model of spatial transport. *A&A* **686**, A219.

ELMEGREEN, B.G. & SCALO, J. 2004 Interstellar turbulence I: observations and processes. *ARA&A* **42**, 211–273.

ELS, P. L., ENGELBRECHT, N. E., LANG, J. T. & STRAUSS, R. D. 2024 The diffusion tensor of protons at 1 au: comparing simulation, observation, and theory. *ApJ* **975**, 134.

ENGELBRECHT, N.E., EFFENBERGER, F., FLORINSKI, V., POTGIETER, M. S., RUFFOLO, D., CHHIBER, R., USMANOV, A. V., RANKIN, J. S. & ELS, P. L. 2022 Theory of cosmic ray transport in the heliosphere. *Space Sci. Rev.* **218**, 33.

EWART, R.J., REICHHERZER, P., BOTT, A.F.A., KUNZ, M.W. & SCHEKOCHIHIN, A.A. 2024 Cosmic-ray confinement in radio bubbles by micromirrors. *MNRAS* **532**, 2098–2107.

FERNÁNDEZ, D. & Paola. 2020 Magnetic fields in the intracluster medium *PhD thesis*, University of Hamburg.

GALISHNIKOVA, A.K., KUNZ, M.W. & SCHEKOCHIHIN, A.A. 2022 Tearing instability and current-sheet disruption in the turbulent dynamo. *Phys. Rev. X* **12**, 041027.

GENT, F.A., LOW, M., Mordecai-Mark, & KORPI-LAGG, M.J. 2024 Transition from small-scale to large-scale dynamo in a supernova-driven, Multiphase Medium. *ApJ* **961**, 7.

GRAFKE, T., GRAUER, R. & SCHÄFER, T. 2015 The instanton method and its numerical implementation in fluid mechanics. *J. Phys. A Math. Theor.* **48**, 333001.

GRAUER, R., KRUG, J. & MARLIANI, C. 1994 Scaling of high-order structure functions in magnetohydrodynamic turbulence. *Phys. Lett. A* **195**, 335–338.

GRAUER, R. & MARLIANI, C. 2000 Current-sheet formation in 3D ideal incompressible magnetohydrodynamics. *Phys. Rev. Lett.* **84**, 4850–4853.

GROŠELJ, D., CHEN, C.H.K., MALLET, A., SAMTANEY, R., SCHNEIDER, K. & JENKO, F. 2019 Kinetic turbulence in astrophysical plasmas: waves and/or structures? *Phys. Rev. X* **9**, 031037.

HAUGEN, N.E.L. & BRANDENBURG, A. 2004 Inertial range scaling in numerical turbulence with hyperviscosity. *Phys. Rev. E* **70**, 026405.

HEAD, T., KUMAR, M., NAHRSTAEDT, H., LOUPPE, G. & SHCHERBATYI, I. 2021 Scikit-optimize/scikit-optimize. *Zenodo*. doi: 10.5281/zenodo.5565057.

HOPKINS, P.F., CHAN, T. K., GARRISON-KIMMEL, S., JI, S., SU, K.-Y., HUMMELS, C.B., KEREŠ, D., QUATAERT, E. & FAUCHER-GIGUÈRE, C.-A. 2020 But what about: cosmic rays, magnetic fields, conduction, and viscosity in galaxy formation. *MNRAS* **492**, 3465–3498.

HOPKINS, P.F., SQUIRE, J., BUTSKY, I.S. & JI, S. 2022 Standard self-confinement and extrinsic turbulence models for cosmic ray transport are fundamentally incompatible with observations. *MNRAS* **517**, 5413–5448.

HOSKING, D.N. & SCHEKOCHIHIN, A.A. 2021 Reconnection-controlled decay of magnetohydrodynamic turbulence and the role of invariants. *Phys. Rev. X* **11**, 041005.

HOUDE, M., VAILLANCOURT, J.E., HILDEBRAND, R.H., CHITSAZZADEH, S. & KIRBY, L. 2009 Dispersion of magnetic fields in molecular clouds. II. *ApJ* **706**, 1504–1516.

HUDSON, T. & LI, X.H. 2020 Coarse-graining of overdamped langevin dynamics via the mori–zwanzig formalism. *Multiscale Model. Sim.* **18**, 1113–1135.

JANSSON, R. & FARRAR, G.R. 2012 A new model of the galactic magnetic field. *ApJ* **757**, 14.

JOKIPII, J. R. 1966 Cosmic-ray propagation. I. Charged particles in a random magnetic field. *ApJ* **146**, 480.

KAMAL YOUSSEF, F. R. & GRENIER, I. A. 2024 Cosmic-ray diffusion in two local filamentary clouds. *A&A* **685**, A102.

KEMPSKI, P., FIELDING, D.B., QUATAERT, E., GALISHNIKOVA, A.K., KUNZ, M.W., PHILIPPOV, A.A. & RIPPERDA, B. 2023 Cosmic ray transport in large-amplitude turbulence with small-scale field reversals. *MNRAS* **525**, 4985–4998.

KEMPSKI, P., LI, D., FIELDING, D.B., QUATAERT, E., PHINNEY, E.S., KUNZ, M.W., JOW, D.L. & PHILIPPOV, A.A. 2025 A unified model of cosmic-ray propagation and radio extreme scattering events from intermittent interstellar structures. *ApJ* **990**, L18.

KEMPSKI, P. & QUATAERT, E. 2022 Reconciling cosmic ray transport theory with phenomenological models motivated by Milky-way data. *MNRAS* **514**, 657–674.

KHABAROVA, O., *et al.* 2021 Current sheets, plasmoids and flux ropes in the heliosphere. Part I. 2-D or not 2-d? General and observational aspects. *Space Sci. Rev.* **217**, 38.

KRAPIVSKY, P.L., REDNER, S. & BEN-NAIM, E. 2010 *A Kinetic View of Statistical Physics*. Cambridge University Press.

KULSRUD, R.M. 2005 *Plasma Physics for Astrophysics*. Princeton University Press.

LEMOINE, M. 2021 Particle acceleration in strong MHD turbulence. *Phys. Rev. D* **104**, 063020.

LEMOINE, M. 2023 Particle transport through localized interactions with sharp magnetic field bends in MHD turbulence. *J. Plasma Phys.* **89**, 175890501.

LESAFFRE, P., DURRIVE, J.-B., GOOSSAERT, J., POIRIER, S., COLOMBI, S., RICHARD, P., ALLYS, E. & BETHUNE, W. 2025 Multiscale turbulence synthesis: validation in 2D hydrodynamics. arXiv:2506.23659

LI, T., BIFERALE, L., BONACCORSO, F., SCARPOLINI, M.A. & BUZZICOTTI, M. 2024 Synthetic lagrangian turbulence by generative diffusion models. *Nat. Mach. Intell.* **6**, 393–403.

LIANG, N. & OH, S.P. 2025 Lévy flights and leaky boxes: anomalous diffusion of cosmic rays. *MNRAS* **543**, 1911–1934.

LIN, Y.T., TIAN, Y., LIVESCU, D. & ANGHEL, M. 2021 Data-driven learning for the Mori–Zwanzig formalism: a generalization of the Koopman learning framework. *SIAM J. Appl. Dyn. Syst.* **20**, 2558–2601.

LOUREIRO, N.F. & BOLDYREV, S. 2017 Role of magnetic reconnection in magnetohydrodynamic turbulence. *Phys. Rev. Lett.* **118**, 245101.

LÜBKE, J., EFFENBERGER, F., WILBERT, M., FICHTNER, H. & GRAUER, R. 2024 Towards synthetic magnetic turbulence with coherent structures. *EPL* **146**, 43001.

MACI, D., KEPPENS, R. & BACCHINI, F. 2024 BxC toolkit: generating tailored turbulent 3D magnetic fields. *ApJS* **273**, 11.

MAGDZIARZ, M. & WERON, A. 2007 Competition between subdiffusion and Lévy flights: a Monte Carlo approach. *Phys. Rev. E* **75**, 056702.

MALARA, F., PERRI, S. & ZIMBARDO, G. 2021 Charged-particle chaotic dynamics in rotational discontinuities. *Phys. Rev. E* **104**, 025208.

MALLET, A., SCHEKOCHIHIN, A. A. & CHANDRAN, B. D. G. 2017 Disruption of sheet-like structures in Alfvénic turbulence by magnetic reconnection. *MNRAS* **468**, 4862–4871.

MARTIN, J., LÜBKE, J., LI, T., BUZZICOTTI, M., GRAUER, R. & BIFERALE, L. 2025 Generation of cosmic-ray trajectories by a diffusion model trained on test particles in 3D magnetohydrodynamic turbulence. *ApJS* **277**, 48.

MATTHAEUS, W. H., WAN, M., SERVIDIO, S., GRECO, A., OSMAN, K. T., OUGHTON, S. & DMITRUK, P. 2015 Intermittency, nonlinear dynamics and dissipation in the solar wind and astrophysical plasmas. *Philos. Trans. R. Soc. Lond. Ser. A* **373**, 20140154–20140154.

MERTSCH, P. 2020 Test particle simulations of cosmic rays. *Ap&SS* **365**, 135.

METZLER, R. & KLAFTER, J. 2000 The random walk's guide to anomalous diffusion: a fractional dynamics approach. *Phys. Rep.* **339**, 1–77.

MEYRAND, R., GALTIER, S. & KIYANI, K.H. 2016 Direct evidence of the transition from weak to strong magnetohydrodynamic turbulence. *Phys. Rev. Lett.* **116**, 105002.

MILLER, D. 2019 Alignment and structure in mhd dynamos. PhD thesis, University of Exeter.

MININNI, P. D., POUQUET, A. G. & MONTGOMERY, D. C. 2006 Small-scale structures in three-dimensional magnetohydrodynamic turbulence. *Phys. Rev. Lett.* **97**, 244503.

MINNIE, J., MATTHAEUS, W. H., BIEBER, J. W., RUFFOLO, D. & BURGER, R. A. 2009 When do particles follow field lines? *J. Geophys. Res. (Space Phys.)* **114**, A01102.

MORILLO, J.M.G. & ALEXAKIS, A. 2025 Magnetic reconnection, plasmoids and numerical resolution. *J. Fluid Mech.* **1007**, R3.

NEUER, M. & SPATSCHEK, K.H. 2006 Diffusion of test particles in stochastic magnetic fields for small Kubo numbers. *Phys. Rev. E* **73**, 026404.

NTORMOUSI, E., VLAHOS, L., KONSTANTINOU, A. & ISLIKER, H. 2024 Strong turbulence and magnetic coherent structures in the interstellar medium. *A&A* **691**, A149.

PARKER, E. N. 1965 The passage of energetic charged particles through interplanetary space. *Planet. Space Sci.* **13**, 9–49.

PEREZ, J.C. & BOLDYREV, S. 2009 Role of Cross-helicity in magnetohydrodynamic turbulence. *Phys. Rev. Lett.* **102**, 025003.

PEZZI, O. & BLASI, P. 2024 Galactic cosmic ray transport in the absence of resonant scattering. *MNRAS* **529**, L13–L18.

PEZZI, O., BLASI, P. & MATTHAEUS, W.H. 2022 Relativistic particle transport and acceleration in structured plasma turbulence. *ApJ* **928**, 25.

PFROMMER, C., PAKMOR, R., SCHAAL, K., SIMPSON, C. M. & SPRINGEL, V. 2017 Simulating cosmic ray physics on a moving mesh. *MNRAS* **465**, 4500–4529.

POLITANO, H. & POUQUET, A. 1995 Model of intermittency in magnetohydrodynamic turbulence. *Phys. Rev. E* **52**, 636–641.

PUCCI, F., MALARA, F., PERRI, S., ZIMBARDO, G., SORRISO-VALVO, L. & VALENTINI, F. 2016 Energetic particle transport in the presence of magnetic turbulence: influence of spectral extension and intermittency. *MNRAS* **459**, 3395–3406.

PUGLIESE, F., BRODIANO, M., ANDRÉS, N. & DMITRUK, P. 2023 Energization of charged test particles in magnetohydrodynamic fields: waves versus turbulence picture. *ApJ* **959**, 28.

QIN, G., MATTHAEUS, W. H. & BIEBER, J. W. 2002 Perpendicular transport of charged particles in composite model turbulence: recovery of diffusion. *ApJ* **578**, L117–L120.

REICHHERZER, P., BECKER TJUS, J., ZWEIBEL, E. G., MERTEN, L. & PUESCHEL, M. J. 2020 Turbulence-level dependence of cosmic ray parallel diffusion. *MNRAS* **498**, 5051–5064.

REICHHERZER, P., BOTT, A.F.A., EWART, R.J., GREGORI, G., KEMPSKI, P., KUNZ, M.W. & SCHEKOCHIHIN, A.A. 2025 Efficient micromirror confinement of sub-teraelectronvolt cosmic rays in galaxy clusters. *Nat. Astron.* **9**, 438–448.

RIEDER, M. & TEYSSIER, R. 2017 A small-scale dynamo in feedback-dominated galaxies – iI. The saturation phase and the final magnetic configuration. *MNRAS* **471**, 2674–2686.

RINCON, F. 2019 Dynamo theories. *J. Plasma Phys.* **85**, 205850401.

RIPPERDA, B., BACCHINI, F., TEUNISSEN, J., XIA, C., PORTH, O., SIRONI, L., LAPENTA, G. & KEPPENS, R. 2018 A comprehensive comparison of relativistic particle integrators. *ApJS* **235**, 21.

ROBITAILLE, J. F., ABDELDAYEM, A., JONCOUR, I., MORAUX, E., MOTTE, F., LESAFFRE, P. & KHALIL, A. 2020 Statistical model for filamentary structures of molecular clouds. The modified multiplicative random cascade model and its multifractal nature. *A&A* **641**, A138.

RYU, D., SCHLEICHER, D. R. G., TREUMANN, R. A., TSAGAS, C. G. & WIDROW, L. M. 2012 Magnetic fields in the large-scale structure of the universe. *Space Sci. Rev.* **166**, 1–35.

SAMPSON, M.L., BEATTIE, J.R., KRUMHOLZ, M.R., CROCKER, R.M., FEDERRATH, C. & SETA, A. 2023 Turbulent diffusion of streaming cosmic rays in compressible, partially ionized plasma. *MNRAS* **519**, 1503–1525.

SCHEKOCHIHIN, A.A. 2022 MHD turbulence: a biased review. *J. Plasma Phys.* **88**, 155880501.

SCHEKOCHIHIN, A.A., COWLEY, S.C., TAYLOR, S.F., MARON, J.L. & MCWILLIAMS, J.C. 2004 Simulations of the small-scale turbulent dynamo. *ApJ* **612**, 276–307.

SCHEKOCHIHIN, A.A., MARON, J.L., COWLEY, S.C. & MCWILLIAMS, J.C. 2002 The small-scale structure of magnetohydrodynamic turbulence with large magnetic Prandtl numbers. *ApJ* **576**, 806–813.

SCHLICKEISER, R. 2002 *Cosmic Ray Astrophysics*. Springer.

SCHORLEPP, T. & GRAFKE, T. 2025 Scalability of the second-order reliability method for stochastic differential equations with multiplicative noise. arXiv:2502.20114

SERVIDIO, S., DMITRUK, P., GRECO, A., WAN, M., DONATO, S., CASSAK, P. A., SHAY, M. A., CARBONE, V. & MATTHAEUS, W. H. 2011 Magnetic reconnection as an element of turbulence. *Nonlinear Proc. Geoph.* **18**, 675–695.

SETA, A., BUSHBY, P.J., SHUKUROV, A. & WOOD, T.S. 2020 Saturation mechanism of the fluctuation dynamo at $\mathrm{Pr}_M \geqslant 1$. *Phys. Rev. Fluids* **5**, 043702.

SHUKUROV, A., SNODIN, A.P., SETA, A., BUSHBY, P.J. & WOOD, T.S. 2017 Cosmic rays in intermittent magnetic fields. *ApJ* **839**, L16.

SIRONI, L., COMISSO, L. & GOLANT, R. 2023 Generation of near-equipartition magnetic fields in turbulent collisionless plasmas. *Phys. Rev. Lett.* **131**, 055201.

SKILLING, J. 1975 Cosmic ray streaming – I. Effect of Alfvén waves on particles. *MNRAS* **172**, 557–566.

ST-ONGE, D.A. & KUNZ, M.W. 2018 Fluctuation dynamo in a collisionless, weakly magnetized plasma. *ApJ* **863**, L25.

STEINWANDEL, U.P., DOLAG, K., BÖSS, L.M. & MARIN-GILABERT, T. 2024 Toward cosmological simulations of the magnetized intracluster medium with resolved coulomb collision scale. *ApJ* **967**, 125.

STRAUSS, R.D.T. & EFFENBERGER, F. 2017 A Hitch–Hiker's guide to stochastic differential equations. Solution methods for energetic particle transport in space physics and astrophysics. *Space Sci. Rev.* **212**, 151–192.

SUBEDI, P., CHHIBER, R., TESSEIN, J. A., WAN, M. & MATTHAEUS, W. H. 2014 Generating synthetic magnetic field intermittency using a minimal multiscale lagrangian mapping approach. *ApJ* **796**, 97.

TU, C. Y. & MARSCH, E. 1995 Magnetohydrodynamic structures waves and turbulence in the solar wind - observations and theories. *Space Sci. Rev.* **73**, 1–210.

VAN DEN BERG, J. P., ELS, P. L. & ENGELBRECHT, N. E. 2024 An evaluation of different numerical methods to calculate the pitch-angle diffusion coefficient from full-orbit simulations: disentangling a rope of sand. *ApJ* **977**, 174.

VAZZA, F., BRUNETTI, G., BRÜGGEN, M. & BONAFEDE, A. 2018 Resolved magnetic dynamo action in the simulated intracluster medium. *MNRAS* **474**, 1672–1687.

VINOGRADOV, A., ALEXANDROVA, O., DÉMOULIN, P., ARTEMYEV, A., MAKSIMOVIC, M., MANGENEY, A., VASILIEV, A., PETRUKOVICH, A.A. & BALE, S. 2024 Embedded coherent structures from magnetohydrodynamics to sub-ion scales in turbulent solar wind at 0.17 au. *ApJ* **971**, 88.

WANG, J., CHHIBER, R., ROY, S., CUESTA, M.E., PECORA, F., YANG, Y., FU, X., LI, H. & MATTHAEUS, W.H. 2024 Anisotropy of density fluctuations in the solar wind at 1 au. *ApJ* **967**, 150.

WEYGAND, J.M., MATTHAEUS, W. H., DASSO, S. & KIVELSON, M. G. 2011 Correlation and Taylor scale variability in the interplanetary magnetic field fluctuations as a function of solar wind speed. *J. Geophys. Res. (Space Phys.)* **116**, A08102.

WEYGAND, J.M., MATTHAEUS, W. H., KIVELSON, M. G. & DASSO, S. 2013 Magnetic correlation functions in the slow and fast solar wind in the Eulerian reference frame. *J. Geophys. Res. (Space Phys.)* **118**, 3995–4004.

WILBERT, M. 2023 Implementation and application of a pseudo-spectral MHD solver combined with an immersed boundary method to support the dresdyn dynamo experiment. PhD thesis, Ruhr-Universität Bochum.

WILBERT, M., GIESECKE, A. & GRAUER, R. 2022 Numerical investigation of the flow inside a precession-driven cylindrical cavity with additional baffles using an immersed boundary method. *Phys. Fluids* **34**, 096607.

XU, S. & YAN, H. 2013 Cosmic-ray parallel and perpendicular transport in turbulent magnetic fields. *ApJ* **779**, 140.

YANG, Y., WAN, M., MATTHAEUS, W.H., SHI, Y., PARASHAR, T.N., LU, Q. & CHEN, S. 2019 Role of magnetic field curvature in magnetohydrodynamic turbulence. *Phys. Plasmas* **26**, 072306.

ZABURDAEV, V., DENISOV, S. & KLAFTER, J. 2015 Lévy walks. *Rev. Mod. Phys.* **87**, 483–530.

ZHANG, C. & XU, S. 2024 Cosmic ray diffusion in magnetic fields amplified by nonlinear turbulent dynamo. *ApJ* **975**, 65.

ZHDANKIN, V., BOLDYREV, S. & UZDENSKY, D.A. 2016 Scalings of intermittent structures in magneto-hydrodynamic turbulence. *Phys. Plasmas* **23**, 055705.

ZHOU, M., ZHDANKIN, V., KUNZ, M.W., LOUREIRO, N.F. & UZDENSKY, D.A. 2024 Magnetogenesis in a collisionless plasma: from Weibel instability to turbulent dynamo. *ApJ* **960**, 12.

ZIMBARDO, G. & PERRI, S. 2020 Non-Markovian pitch-angle scattering as the origin of particle superdiffusion parallel to the magnetic field. *ApJ* **903**, 105.